Received: 19 October 2020 | Revised: 29 January 2021 | Accepted: 13 February 2021

DOI: 10.1002/cnm.3451

RESEARCH ARTICLE - APPLICATION

WILEY

A highly parallel simulation of patient-specific hepatic flows

Zeng Lin[1,2] | **Rongliang Chen**[1,2] | **Beibei Gao**[3] | **Shanlin Qin**[1] | **Bokai Wu**[1] | **Jia Liu**[1,2] | **Xiao-Chuan Cai**[4]

[1]Shenzhen Institutes of Advanced Technology, Chinese Academy of Sciences, Shenzhen, China

[2]Shenzhen Key Laboratory for Exascale Engineering and Scientific Computing, Shenzhen, China

[3]Department of Cardiology, Affiliated Hangzhou First People's Hospital, Zhejiang University School of Medicine, Hangzhou, China

[4]Department of Mathematics, University of Macau, Macau, China

Correspondence
Xiao-Chuan Cai, Department of Mathematics, University of Macau, Macau, China.
Email: xccai@um.edu.mo
Rongliang Chen, Shenzhen Institutes of Advanced Technology, Chinese Academy of Sciences, Shenzhen 518055, China.
Email: rl.chen@siat.ac.cn

Funding information
China Postdoctoral Science Foundation, Grant/Award Number: 2020M682960; National Key R&D Program of China, Grant/Award Number: 2018YFE0198400; National Natural Science Foundation of China, Grant/Award Numbers: 11801543, 81871447; Shenzhen grant, Grant/Award Number: ZDSYS201703031711426; SIAT Innovation Program for Excellent Young Researchers

Abstract

Computational hemodynamics is being developed as an alternative approach for assisting clinical diagnosis and treatment planning for liver diseases. The technology is non-invasive, but the computational time could be high when the full geometry of the blood vessels is taken into account. Existing approaches use either one-dimensional model of the artery or simplified three-dimensional tubular geometry in order to reduce the computational time, but the accuracy is sometime compromised, for example, when simulating blood flows in arteries with plaque. In this work, we study a highly parallel method for the transient incompressible Navier–Stokes equations for the simulation of the blood flows in the full three-dimensional patient-specific hepatic artery, portal vein and hepatic vein. As applications, we also simulate the flow in a patient with hepatectomy and calculate the S (PPG). One of the advantages of simulating blood flows in all hepatic vessels is that it provides a direct estimate of the PPG, which is a gold standard value to assess the portal hypertension. Moreover, the robustness and scalability of the algorithm are also investigated. A 83% parallel efficiency is achieved for solving a problem with 7 million elements on a supercomputer with more than 1000 processor cores.

KEYWORDS

domain decomposition, finite element, hepatectomys, hepatic hemodynamics, parallel computing, patient-specific artery–vein

1 | INTRODUCTION

Liver is the largest gland in the body, weighing around 1.5 kilogram in normal adults.[1] It is an important as well as structurally and functionally complex organ receiving nutrients and other molecules from the intestines before the blood flows back to the heart via the inferior vena cava (IVC). The liver is supplied by two main blood vessels on its right lobe: the hepatic artery and the portal vein (see Figure 1). The hepatic portal vein which carries blood from the spleen, pancreas and intestines contributes about 75% of the blood volume to the liver. This blood is rich in nutrients but relatively poor in oxygen. The hepatic artery, a branch of the celiac trunk from the abdominal aorta, contributes

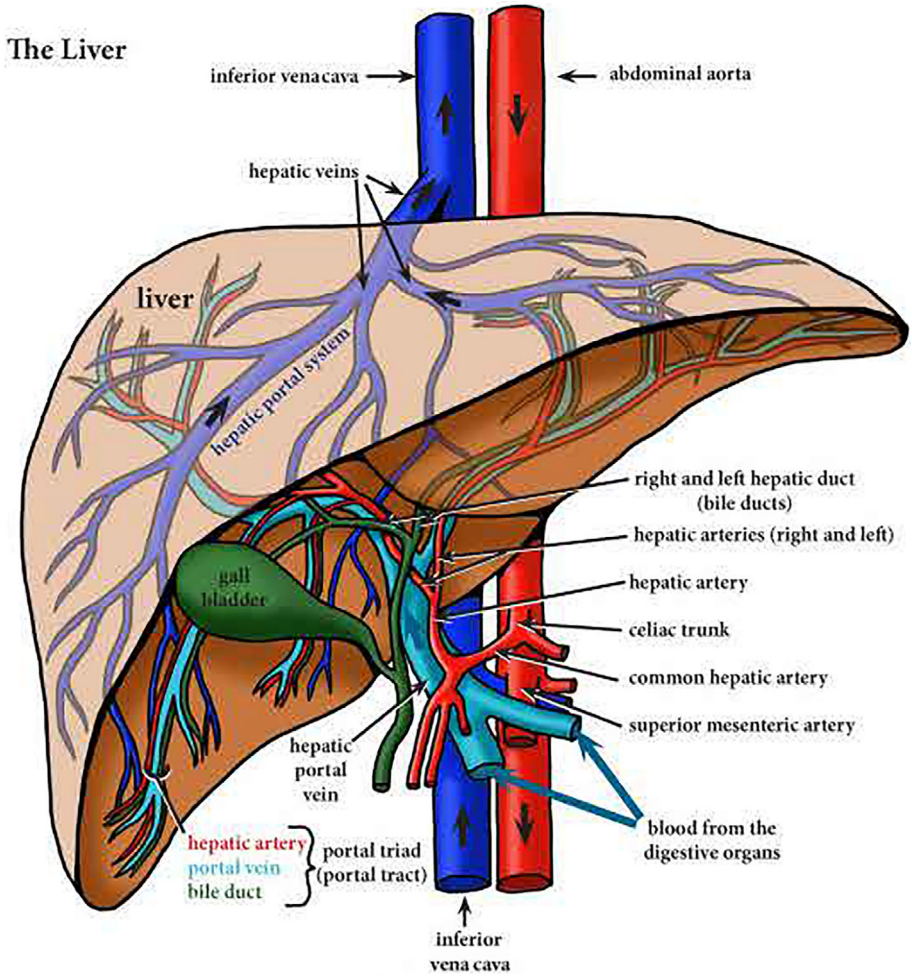

FIGURE 1 The structures of hepatic vessels[2]

about 25% of blood volume to the liver. This blood is well oxygenated but relatively poor in nutrient. The hepatic arteries mix as they enter and pass through the liver lobules, the classical structural unit of the liver, then percolate through the lobules and are collected by the central vein. Central veins unite to form larger sublobular veins, which ultimately join the hepatic veins for the blood to flow back to the heart.

Liver diseases are the major cause of illness and death worldwide,[3] and they are difficult to prevent and diagnose. One of the main difficulties is the measuring of certain hemodynamic values, such as the portal pressure gradient (PPG, the difference in the blood pressure between the portal vein and the IVCSS[4]). PPG is a gold standard to assess the portal hypertension, which is a frequent syndrome and usually caused by chronic liver diseases. Direct measurement of the portal pressure can be performed through transhepatic or transvenous catheterization of the portal vein. This technique further requires catheterizing the IVC to determine the PPG. Because of the risk of intraperitoneal bleeding, direct measurement of the portal pressure is rarely performed and is limited to selected cases of presinusoidal portal hypertension. The measurement of hepatic venous pressure gradient [HVPG, the difference between the wedged hepatic venous pressure (WHVP) and the free hepatic venous pressure (FHVP)] is a safe and reproducible technique that is the preferred way of measuring the PPG in cirrhosis (sinusoidal portal hypertension). In short, the conventional measuring methods are invasive and alternative non-invasive approaches are desirable.

Recently, computational fluid dynamics (CFD) is being investigated as one of the alternative approaches for clinical diagnosis and treatment planning because it is non-invasive. With CFD, one can easily compute several desired pathological values, such as pressure, velocity and wall shear stress (WSS). In the present work, the wall of the vessel is assumed to be rigid. If the deformation of the hepatic vessel is taken into consideration, a fluid–structure interaction (FSI) algorithm would be necessary.[5] However, it is difficult to obtain the thickness and material properties of the

vascular wall, such as the Young's modulus and Poisson ratio. Without such information the results from the FSI computation maybe worse than the fluid-only simulation. Therefore, we focus on the fluid-only simulation in this work.

To compute the hepatic blood perfusion there are two major classes of techniques, one uses a one-dimensional (1D) model of the arterial network and the other is based on a three-dimensional (3D) model of the arterial network. The 1D method is fast and easy to implement and is able to reproduce 3D results on a small portion of the artery.[6] To obtain more realistic results for the whole liver, 3D patient-specific arterial geometry segmented from magnetic resonance imaging (MRI) or computed tomography (CT) are required. Although the computational cost is higher, the 3D simulation is essential for capturing certain flow properties such as recirculation zones, etc. The aim of the paper is to introduce an algorithmic framework for the simulation of blood flows in full 3D patient-specific hepatic vessels on parallel computers with a targeting computing time of a few hours.

There are several existing works on the numerical simulation of hepatic perfusion. For instance, Ho et al[7] developed a 3D flow model with a 1D circulation model for the hemodynamic analysis of the transjugular intrahepatic portosystemic shunt (TIPS) and gave a quantitative analysis of the interplay between TIPS and the hepatic flows. The 3D model is used only for a small portion of the artery. More recently in 2019,[8] the group uses a much larger 3D model in which all vessels are assumed to be tubes to simulate blood flows in the human hepatic artery, the portal vein, and the hepatic vein. Using the same geometry as in Reference 8 that has a tree structure similar to the human liver, but non-patient-specific geometry for each segment, Ma et al[9] computed the blood flows in living liver donor after the left hepatectomy. Although the simplified one-dimensional Navier–Stokes equation can significantly reduce the computational time, the numerical accuracy is sometime compromised. For example, when the artery is partially blocked due to a plaque, the flow becomes truly three-dimensional, neither the one-dimensional model nor the three-dimensional tube model can provide the correct flow field. To gain insight on the microsphere transport in a hepatic artery system, Basciano et al[10] studied the influence of some parameters on the transport. Aramburu et al[11] presented a numerical simulation for the liver radioembolization pretreatment and also the actual treatment under different scenarios. Subsequently, Aramburu et al[12] studied a patient-specific truncated hepatic artery to analyze the influence of a microcatheter with an angled tip. Yin et al[13] studied the morphometry and hemodynamic performance of abdominal aorta with two major branches of the hepatic artery. Sheu et al[14] utilized a coupled heat transfer and Navier–Stokes system to investigate the factors that may affect the radio-frequency heating characteristics of the liver with three branches of the artery for the hepatocellular carcinoma and metastatic liver tumors. A diffuse interface method for coupling free and porous-medium-type flows modeled by the Navier–Stokes and Darcy equations is presented by Stoter et al[15] to compute the perfusion profile for a full-scale 3D human liver. To the best of our knowledge the present paper is the first work that simulates the blood flow in a full-size patient-specific hepatic system with all three hepatic vessels. One of the advantages of integrating the perfusion in all hepatic vessels is that it provides the PPG, which is a gold standard value to judge the reliability of the clinically measured hepatic venous pressure gradient that is often used to substitute the portal venous pressure which is difficult to measure clinically.

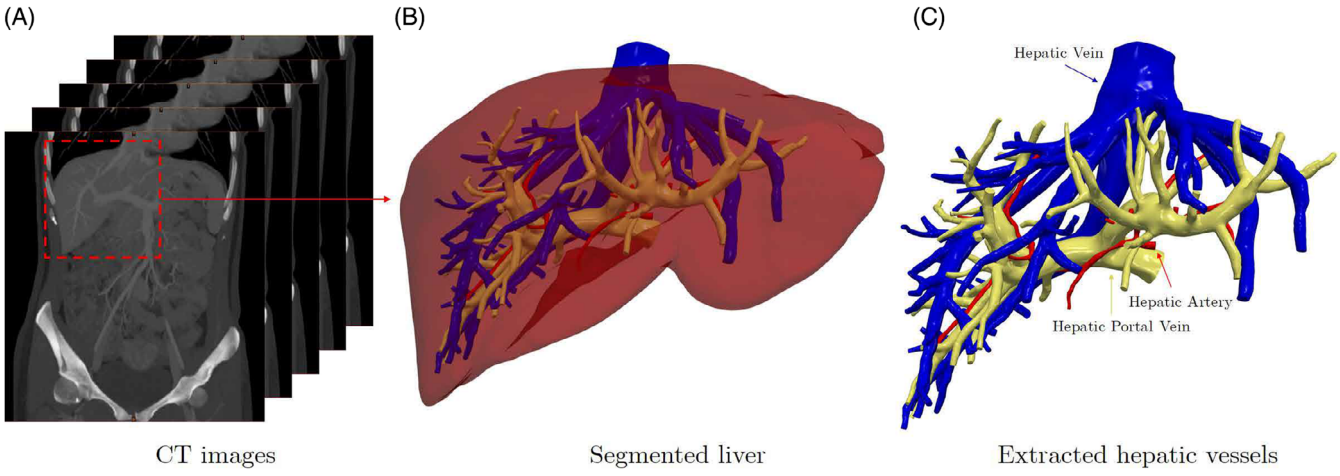

FIGURE 2 Illustration of the steps to extract the patient-specific hepatic artery, hepatic portal vein and hepatic vein from the CT images

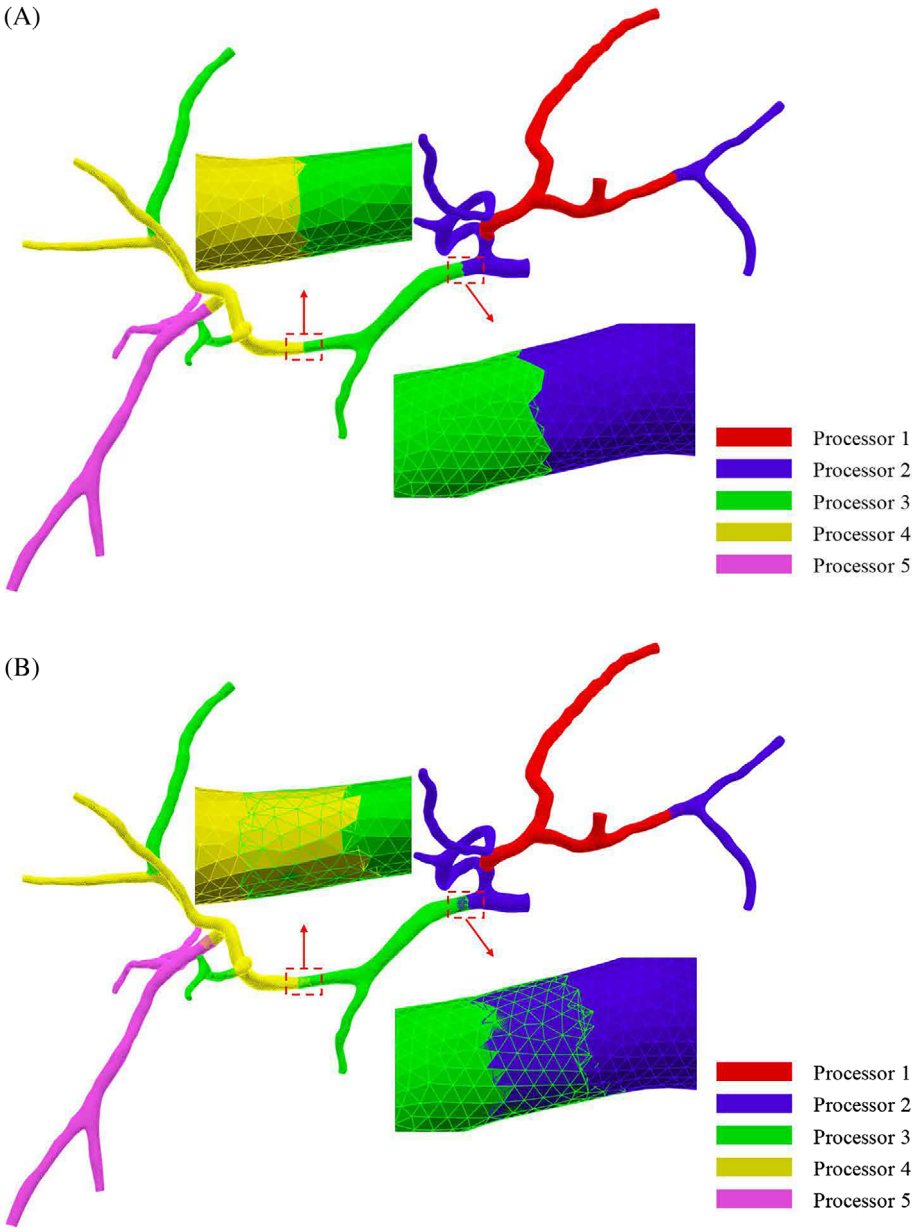

FIGURE 3 The left figure shows a partition of the global mesh into five non-overlapping sub-meshes. The right figure shows the corresponding overlapping partition. Note that some sub-meshes may have pieces of the artery that are not connected (for example, the three green pieces belong to the same sub-mesh, therefore, are mapped to the same processor)

One of the challenges of the numerical simulation of patient-specific 3D hepatic blood flows is the high computational cost. Most of existing works are based on commercial software packages, such as ANSYS CFX and Fluent (ANSYS Inc.) that are easy to use but the parallelism is often limited. For instance, ANSYS is scalable only to a few hundred processor cores, which is acceptable for simulating steady-state problems and problems with a small number of degrees of freedom. For unsteady problems with realistic geometry discretized into a system with a few million of degree of freedoms, it often takes days of wall clock time to obtain results in a full cardiac cycle. We mention that ANSYS uses a finite volume method to solve the governing equations, while in this paper we use a finite element method.

A highly parallel solver is needed to simulate large 3D problems. There are several recent publications devoted to the development of parallel algorithms for blood flow simulations. For example, Kong et al[16] developed a scalable parallel domain decomposition method to investigate an unsteady blood flow problem that works well on a supercomputer with up to 10,000 processor cores. Later, Kong et al[5] extended the method to solve a monolithically coupled fluid–

FIGURE 4 The pulsatile velocity profiles for one cardiac cycle

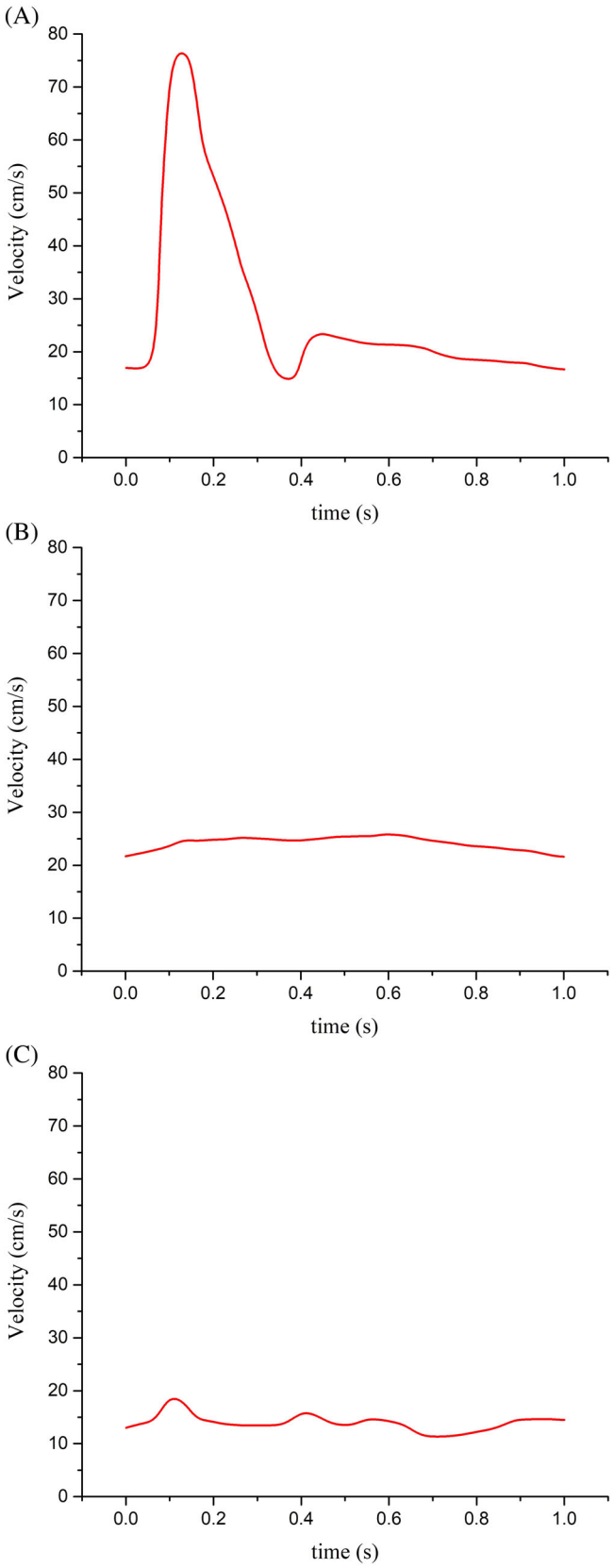

structure system for the modeling the interaction of blood flow and arterial wall in a patient-specific compliant pulmonary artery. A multi-scale calculation of the blood flow in a network consisting of all the primary arteries in a human body is presented by Xiao et al.[17] Forti et al[18] studied the scalability of a large-scale nonconforming FSI based simulation of a patient-specific arterial bypass.

In this work, we study an efficient and highly parallel finite element method based on domain decomposition method for the Navier–Stokes equations.[5,16,19-21] With the method, a simulation of a full 3D patient-specific hepatic flow on a mesh with around 10 million elements can be accomplished in a few hours. Precisely speaking, the domain decomposition algorithm partitions the hepatic vessels into a large number of sub-vessels that are mapped onto different processor cores of the parallel computer. In the overlapping domain decomposition method,[22,23] the submeshes are extended to overlap with their neighboring submeshes. The partition is obtained via ParMETIS/METIS.[24] The algorithm has several algebraic components including an inexact Newton method[25] that solves the system of nonlinear equations. During each Newton iteration, the solution of the Jacobian system is obtained by using a Krylov subspace method[26] preconditioned by a scalable Schwarz preconditioner.[27] The algorithms are implemented on a supercomputer with more than 1000 processor cores and the parallel efficiency that higher than 80% for all the experiments is achieved, which illustrates that our methods are suitable for the hepatic blood vessels. Moreover, we also simulate successfully a flow in a patient with hepatectomy.

The layout of this paper is as follows. The mathematical model for the hepatic flow, its stabilized finite element discretization and a parallel algebraic solver are described in Section 2. In Section 3, numerical experiments for a full-size patient-specific liver are presented. A flow in the portal vein after the left hepatectomy is computed and discussed in detail. The PPG values at some sample pairs of points are also calculated. Finally, conclusions and discussion are drawn in Section 4.

2 | METHODS

2.1 | Mathematical model

In this study, we consider the numerical simulation of blood flows in the liver including the hepatic artery, the hepatic portal vein and the hepatic vein. Figure 2 depicts the main steps to obtain the geometry of the triple vessels. From the CT images in Figure 2A, the hepatic tissue and the main hepatic vessels are segmented as plotted in Figure 2B. Then the geometry of the hepatic artery, hepatic portal vein and hepatic vein are extracted as shown in Figure 2C. The

TABLE 1 Physiological ranges of hepatic hemodynamics

Parameter	Range	Unit
Hepatic arterial pressure[31]	70–110	mmHg
Hepatic arterial peak-systolic velocity[32]	43–67	cm/s
Hepatic arterial end-diastolic velocity[32]	12–20	cm/s
Portal venous pressure[33]	6–10	mmHg
Portal venous peak-systolic velocity[34]	20–40	cm/s
Portal venous end-diastolic velocity[34]	≤ 16	cm/s
Hepatic venous pressure gradient (HVPG)[35]	≤ 5	mmHg

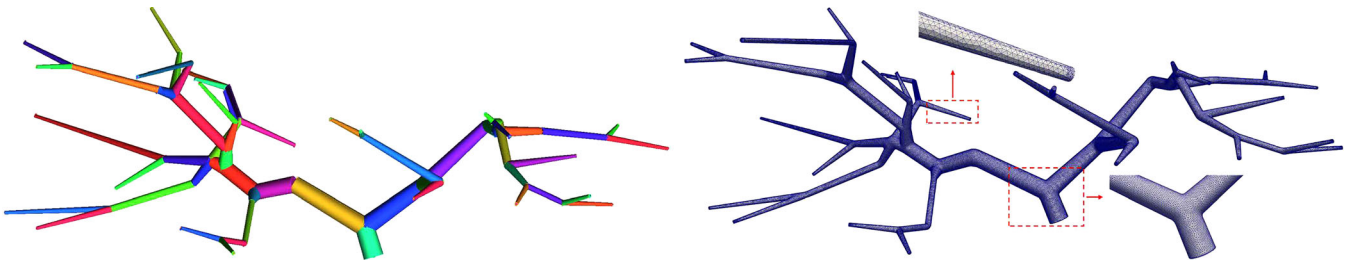

FIGURE 5 A benchmark hepatic artery re-constructed using geometric information from Reference 8 (left figure) and its finite element mesh (right figure)

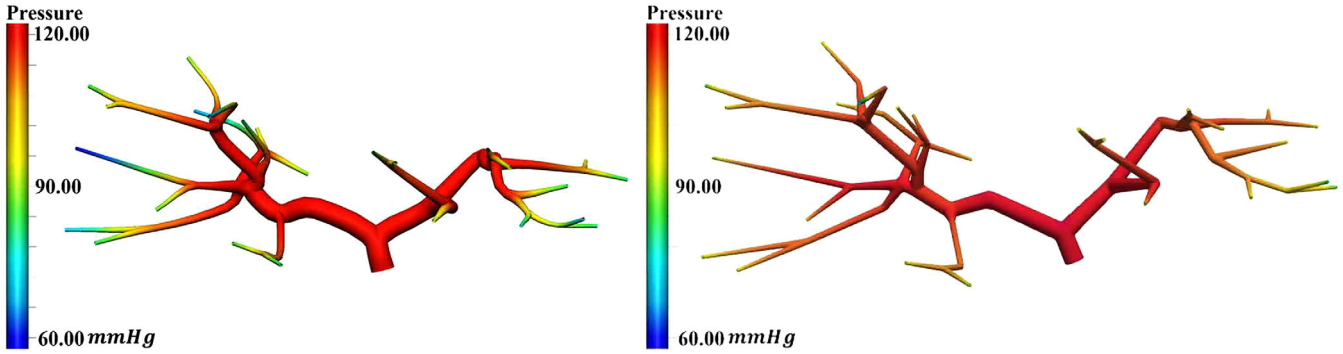

FIGURE 6 A comparison of the computed pressure in the benchmark hepatic artery. The left figure is the result from Reference 8, and the right figure is from the proposed method

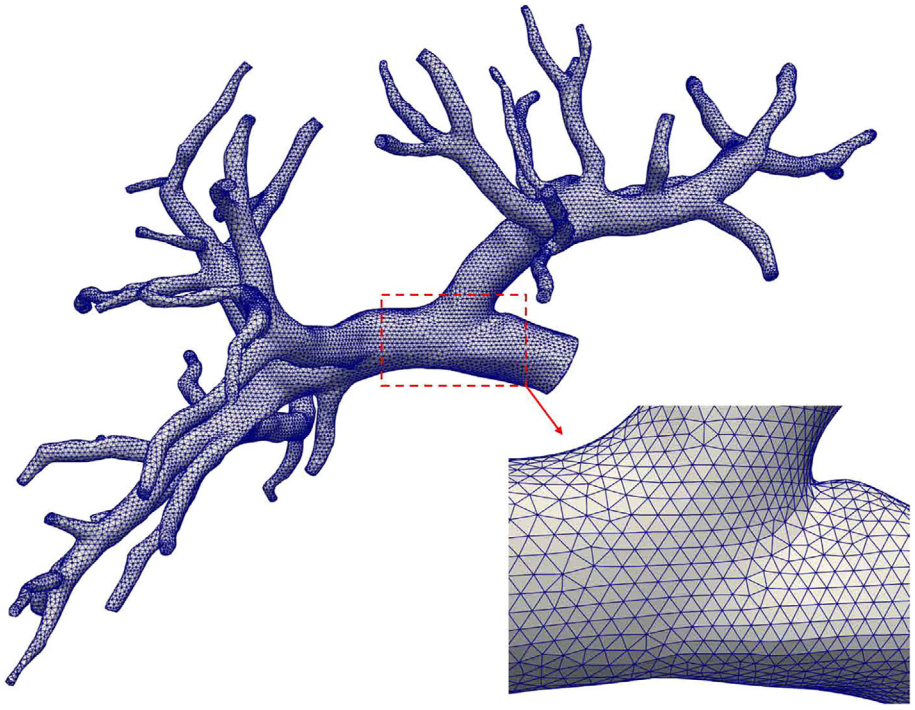

FIGURE 7 A sample finite element mesh for the hepatic portal vein

diameter of the hepatic arterial inlet is 4.2 *mm*, the average diameter of the hepatic arterial outlets is 1.1 *mm*. The diameter of the hepatic portal venous inlet is 18 *mm* and its average diameter of the outlets is 1.8 *mm*. The average diameter of the hepatic venous inlets is 1.5 *mm* and the outlet size is 20 *mm*.

To describe the blood flow in hepatic vessels, we use the unsteady incompressible Navier–Stokes equations:

$$\begin{cases} \rho\dfrac{\partial \boldsymbol{u}(\boldsymbol{x},t)}{\partial t} + \rho(\boldsymbol{u}(\boldsymbol{x},t)\cdot\nabla)\boldsymbol{u}(\boldsymbol{x},t) - \nabla\cdot\boldsymbol{\sigma} = \boldsymbol{f}(\boldsymbol{x},t), (\mathbf{x},t)\in\ \Omega\times(0,T], \\ \nabla\cdot\boldsymbol{u}(\boldsymbol{x},t) = 0, (\boldsymbol{x},t)\in\ \Omega\times(0,T]. \end{cases} \tag{1}$$

Here $\boldsymbol{u}$ denotes the velocity vector, ρ the blood density, $\boldsymbol{f}$ the external force vector and $\boldsymbol{\sigma}$ the Cauchy stress tensor defined as:

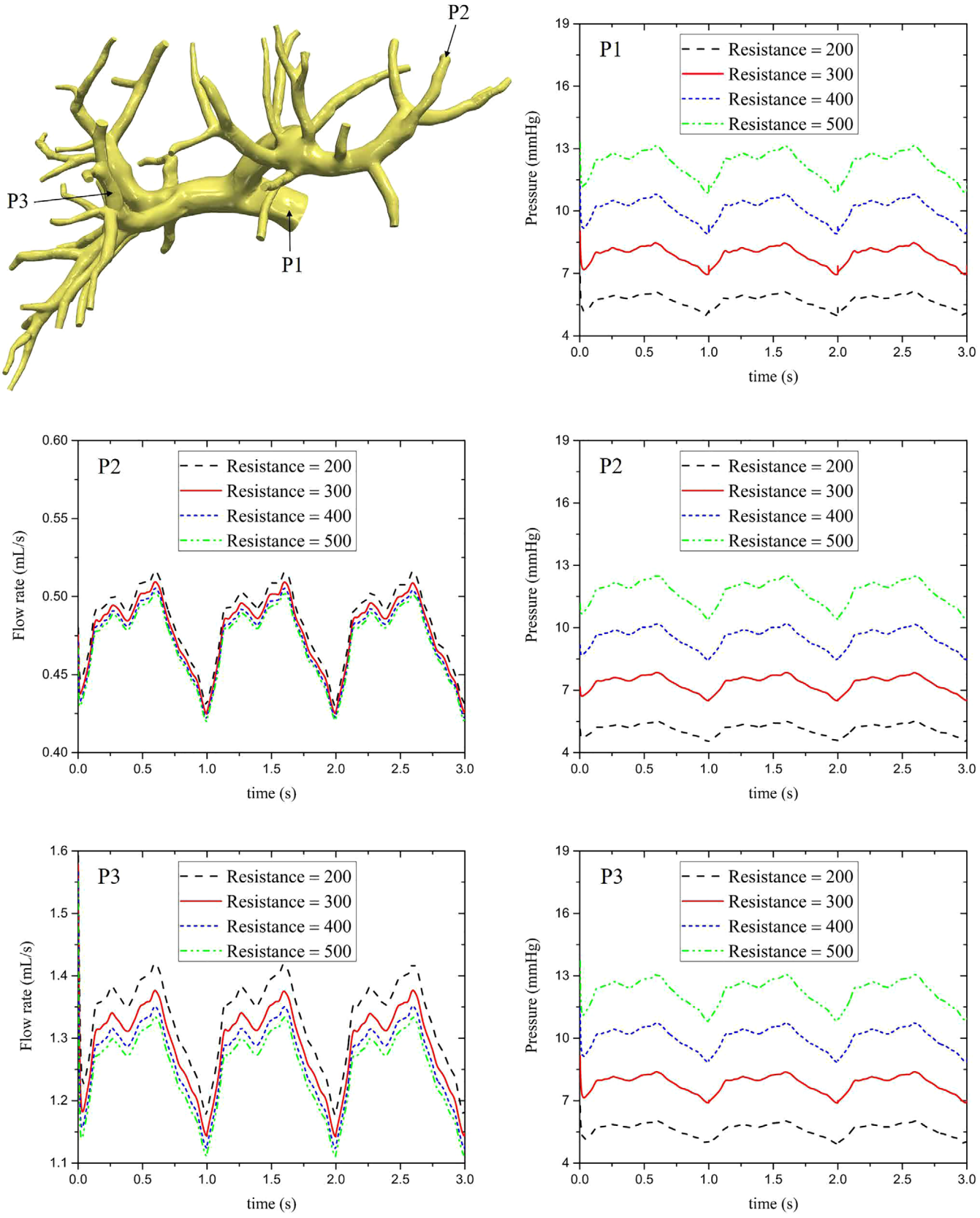

FIGURE 8 A comparison of the computed pressure and flow rate at three selected points with different resistances in the portal vein for three cardiac cycles

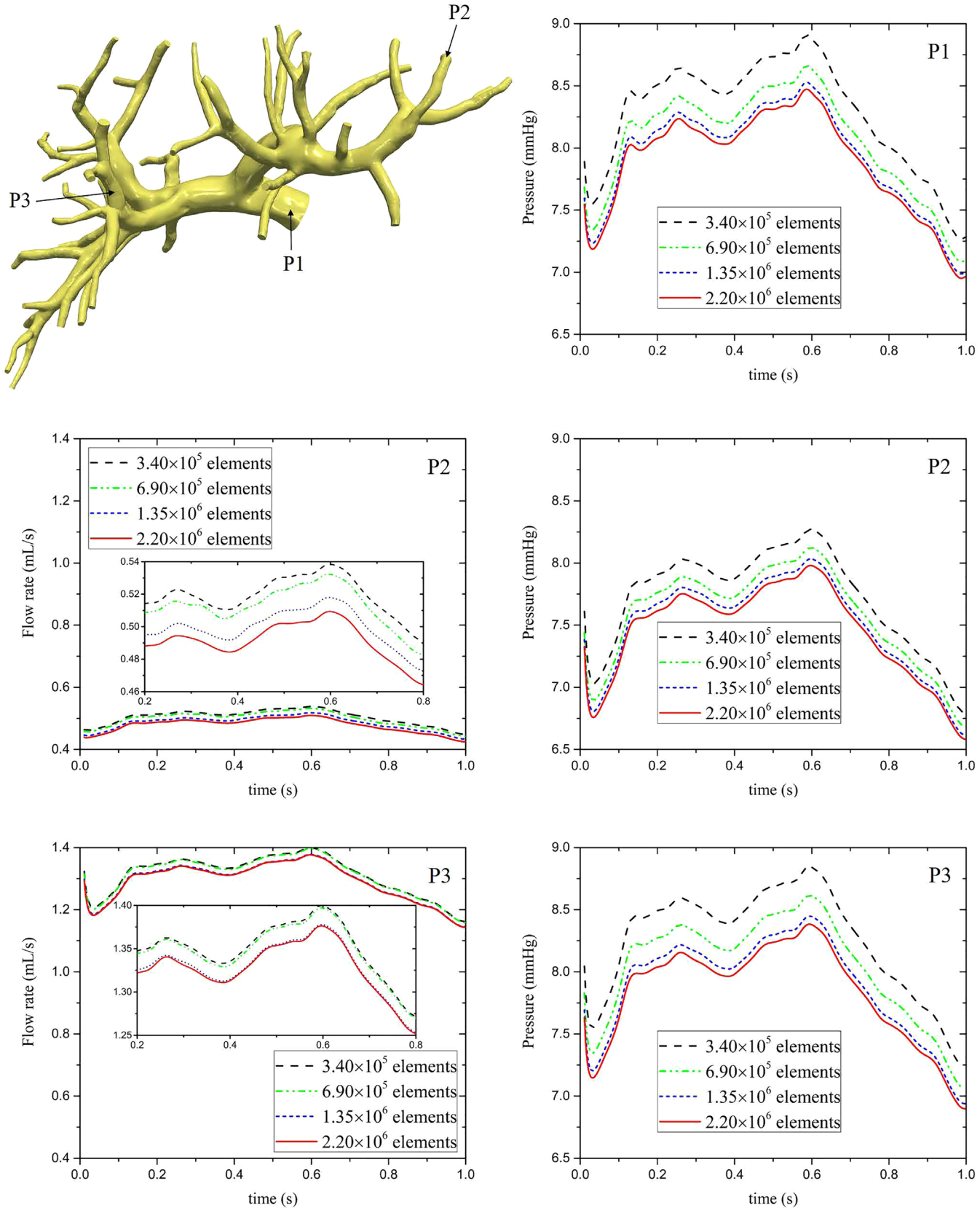

FIGURE 9 A comparison of the computed pressure and flow rate at three selected points with different meshes in the portal vein for a cardiac cycle

Δt (s)	Newton	GMRES	Time (s)	Memory (MB)
5.00×10^{-2}	4.10	171.67	21.06	132.21
1.00×10^{-2}	3.13	160.37	15.85	96.59
5.00×10^{-3}	3.04	139.58	14.59	93.08
1.00×10^{-3}	2.58	99.16	9.75	78.74

Note: The calculations are obtained using 240 processor cores on a mesh with 2.20×10^6 elements. "Time" is the compute time for solving the problems in one time step.

TABLE 2 Performance of the NKS algorithm for different time step sizes

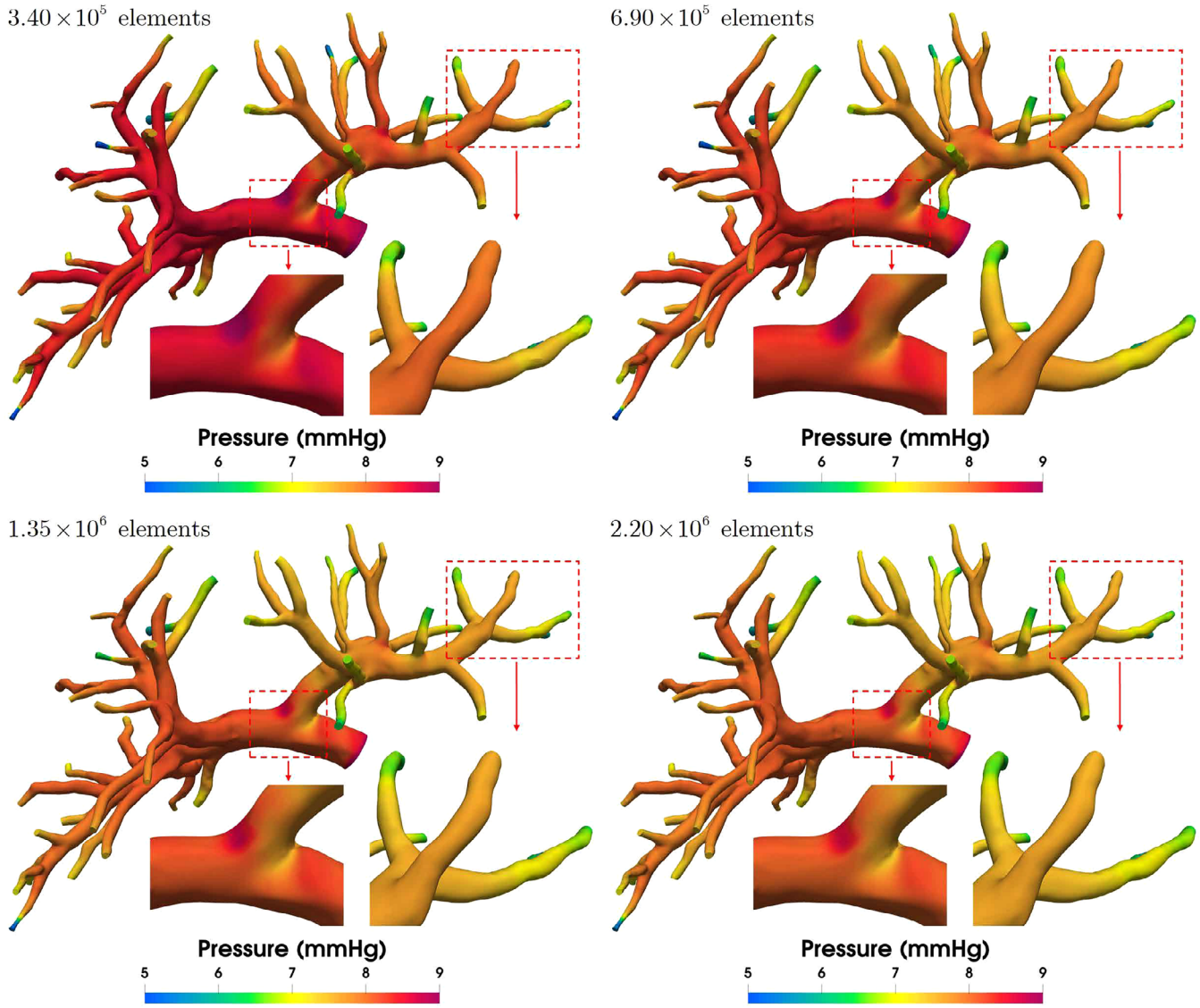

FIGURE 10 The impact of mesh sizes to the computed hepatic portal venous pressure at $t = 0.2\ s$

$$\boldsymbol{\sigma} = -p\boldsymbol{I} + 2\mu\boldsymbol{\varepsilon}(\boldsymbol{u}), \tag{2}$$

where p is the pressure, $\boldsymbol{I}$ is the identity tensor, μ is the dynamic viscosity and $\boldsymbol{\varepsilon}$ is the deformation tensor defined as $\boldsymbol{\varepsilon}(\boldsymbol{u}) = 1/2(\nabla \boldsymbol{u} + \nabla \boldsymbol{u}^T)$.

The initial condition is imposed by

$$\boldsymbol{u}(\boldsymbol{x}, t) = \boldsymbol{u}_0(\boldsymbol{x}, t), t = 0, \boldsymbol{x} \in \Omega, \tag{3}$$

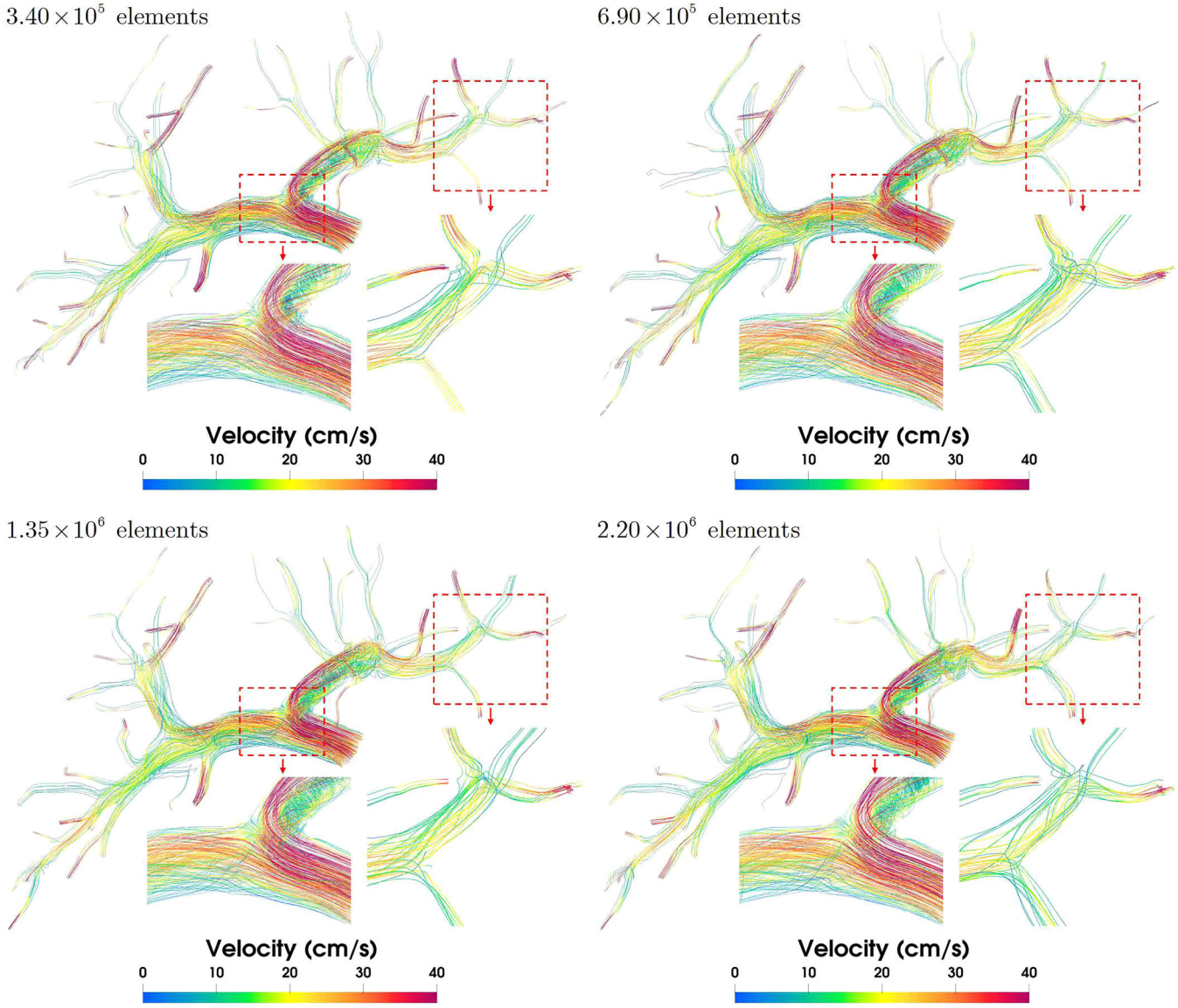

FIGURE 11 The impact of mesh sizes to the computed hepatic portal venous velocity at $t = 0.2\ s$

where $\boldsymbol{u}_0(\boldsymbol{x}, t)$ is the given initial velocity function. For the hepatic artery and the portal vein there exists only one inlet and many outlets. On the other hand, the hepatic vein has many inlets and only one outlet. Thus, two types of boundary conditions are imposed. The boundary conditions for the hepatic artery and portal vein read.[28]

$$\begin{cases} \boldsymbol{u}(\boldsymbol{x},t) = \boldsymbol{u}_I(\boldsymbol{x},t), (\boldsymbol{x},t) \in \Gamma_I \times (0,T], \\ \boldsymbol{u}(\boldsymbol{x},t) = \boldsymbol{0}, (\boldsymbol{x},t) \in \Gamma_W \times (0,T], \\ p_i(\boldsymbol{x},t) = R_i(\boldsymbol{x},t) Q_i(\boldsymbol{x},t), (\boldsymbol{x},t) \in \Gamma_{O_i} \times (0,T], i = 1,2,\cdots,m, \end{cases} \tag{4}$$

where m is the number of outlets, Γ_I is the inlet boundary, Γ_W is the wall boundary and Γ_O is the outlet boundary. The $\boldsymbol{u}_I(\boldsymbol{x}, t)$ is a given inflow velocity profile, $R_i(\boldsymbol{x}, t)$ and $Q_i(\boldsymbol{x}, t)$ are the resistance and flow rate at the i-th outlet, where $Q_i(\boldsymbol{x}, t)$ has the form $Q_i(\boldsymbol{x}, t) = \int_{\Gamma_{O_i}} \boldsymbol{u} \cdot \boldsymbol{n}_i d\Gamma$, where $\boldsymbol{n}_i$ is the outward normal vector of the i-th outlet. In the subsequent calculations, a total resistance R is chosen and each R_i is determined by $R_i = R\left(\sum_{i=1}^{m} S_i^{\frac{3}{2}}\right) / S_i^{\frac{3}{2}}$, here S_i is the area of the i-th outlet surface.[29]

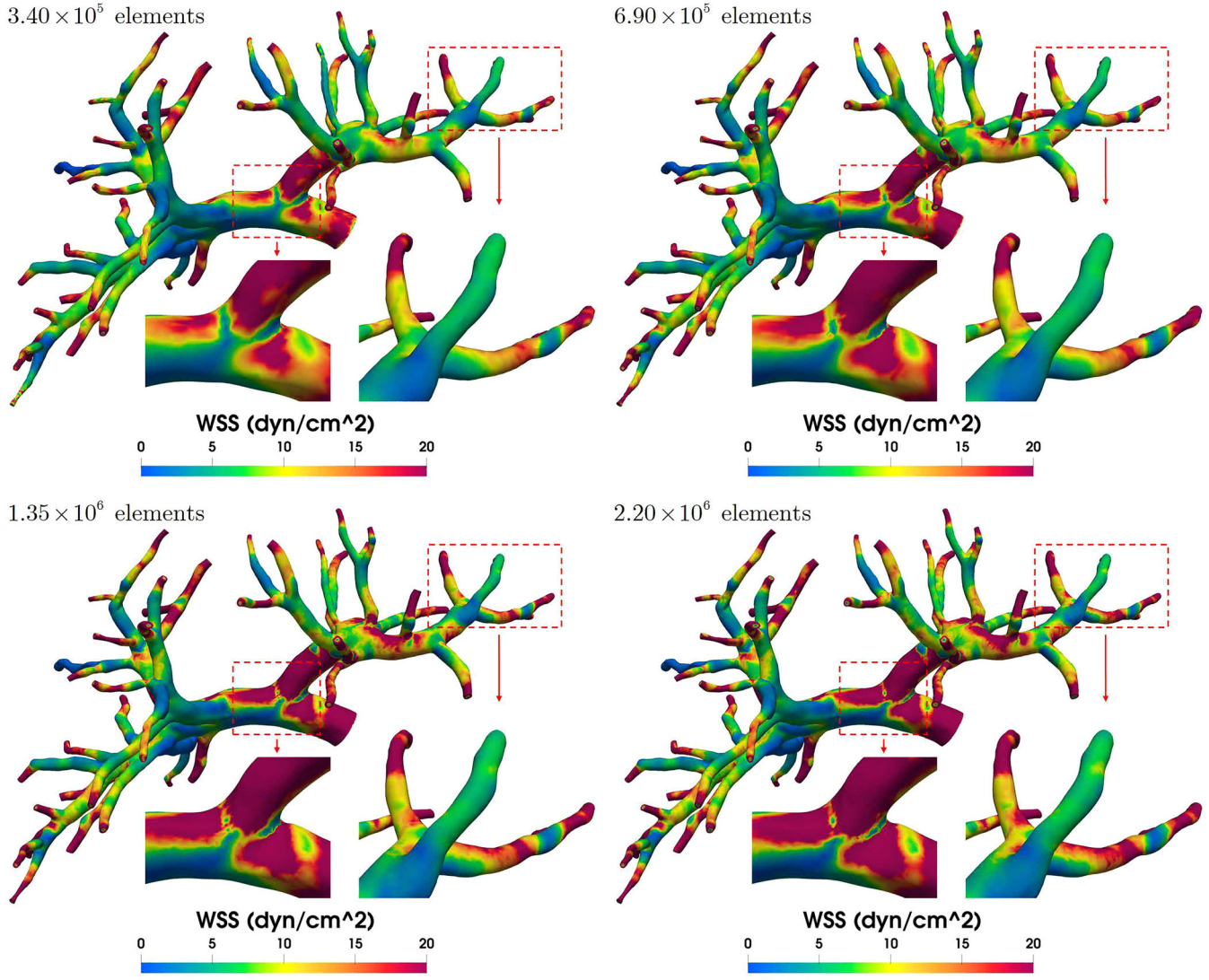

FIGURE 12 The impact of mesh sizes to the computed hepatic portal venous WSS at $t = 0.2\ s$

Similarly, for the hepatic venous that has many inlets and only one outlet, the boundary condition is

$$\begin{cases} \boldsymbol{u}_i(\boldsymbol{x},t) = \boldsymbol{u}_{I_i}(\boldsymbol{x},t), (\boldsymbol{x},t) \in \Gamma_{I_i} \times (0,T], i = 1,2,\cdots,n, \\ \boldsymbol{u}(\boldsymbol{x},t) = \boldsymbol{0}, (\boldsymbol{x},t) \in \Gamma_W \times (0,T], \\ p(\boldsymbol{x},t) = R(\boldsymbol{x},t)Q(\boldsymbol{x},t), (\boldsymbol{x},t) \in \Gamma_O \times (0,T], \end{cases} \tag{5}$$

where n is the number of hepatic vein inlets, other notations are the same as for the aforementioned hepatic artery case.

2.2 | Implicit finite element discretization

We use a piecewise linear continuous finite element method to discretize Equation (1). The weak form of Equation (1) reads: Find $\boldsymbol{u} \in V$ and $p \in P$ such that $\forall \boldsymbol{v} \in V_0$ and $\forall q \in P$,

$$\mathbf{B}(\{\boldsymbol{u},p\},\{\boldsymbol{v},q\}) = 0, \tag{6}$$

where

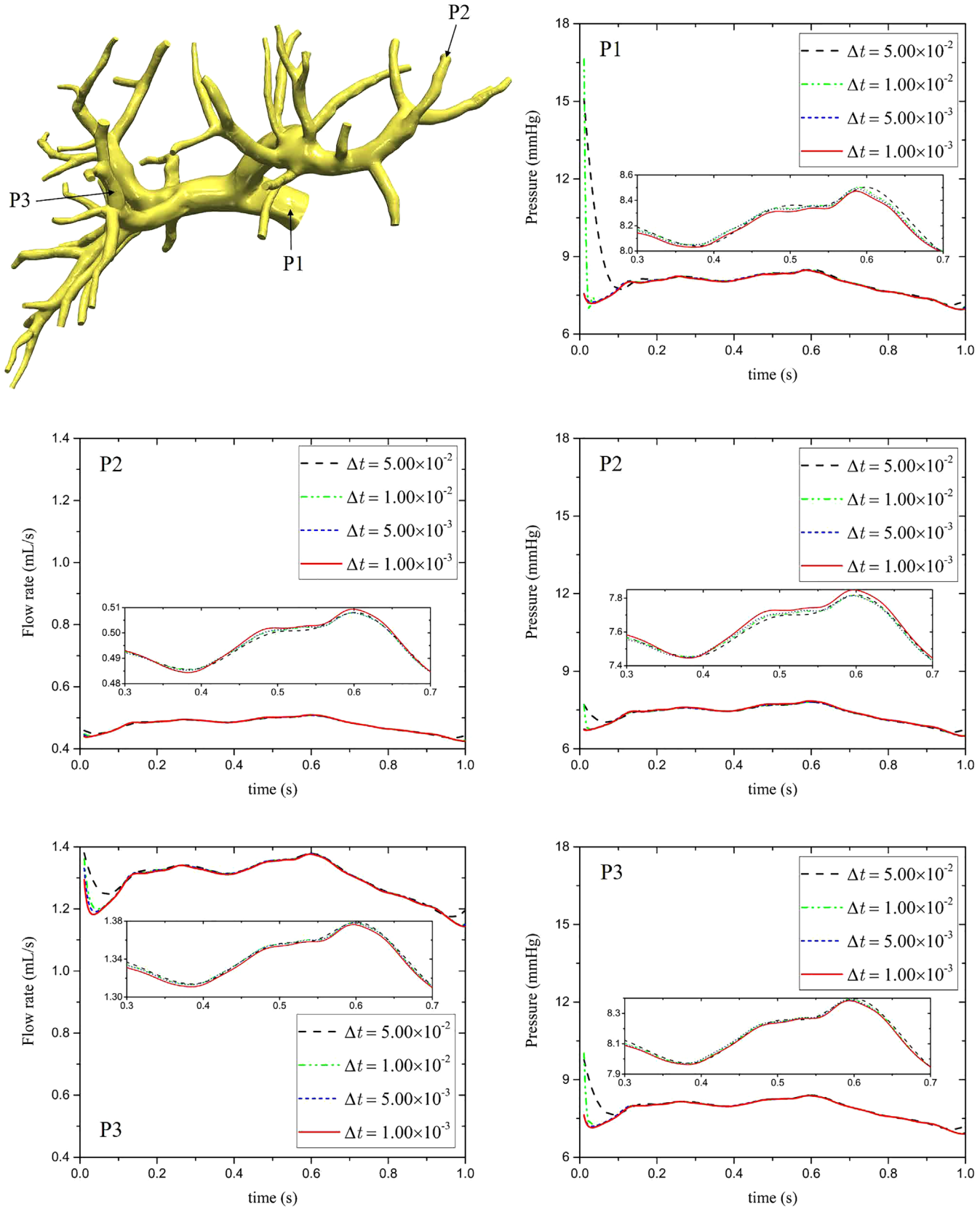

FIGURE 13 A comparison of the computed pressure and flow rate at three selected points with different time step sizes in the portal vein for a cardiac cycle. The zoom-in figures are for $t = 0.3\ s$ to $t = 0.7\ s$

TABLE 3 The influence of the subdomain solvers with various fill-in levels and the overlapping sizes

Subsolver	Overlap	Newton	GMRES	Time (s)	Memory (MB)
ILU(1)	0	3.70	233.84	66.67	352.10
	1	3.70	180.22	59.95	372.29
	2	3.80	170.42	57.75	387.96
	3	3.80	167.92	59.71	394.76
	4	3.80	165.11	60.91	406.10
ILU(2)	0	3.70	214.73	73.22	537.32
	1	3.70	148.14	63.11	566.72
	2	3.70	138.11	59.72	579.17
	3	3.70	133.35	60.28	589.65
	4	3.70	126.38	60.35	609.50
ILU(3)	0	3.70	248.46	97.15	768.00
	1	3.70	129.59	69.02	809.24
	2	3.70	122.19	67.56	828.22
	3	3.70	117.95	69.57	843.41
	4	3.70	108.16	72.72	874.72
ILU(4)	0	3.70	235.32	113.17	1031.56
	1	3.70	130.05	90.39	1085.53
	2	3.70	113.86	83.55	1111.70
	3	3.70	107.70	84.12	1132.85
	4	3.70	98.51	89.06	1176.64

Note: The calculations are carried out on a mesh with 6.99×10^6 elements and the time-step size $\Delta t = 1.00 \times 10^{-3}$ *s*.

TABLE 4 Parallel performance using different number of processor cores

np	Newton	GMRES	Time (s)	Memory (MB)	Speedup	Efficiency
360	3.80	185.24	51.96	265.55	1	100%
720	3.70	179.32	27.84	118.76	1.86	94%
1080	3.70	185.46	20.98	111.94	2.48	83%

Note: The mesh has 6.99×10^6 elements and the time-step size $\Delta t = 1.00 \times 10^{-3}$ *s*.

$$\begin{aligned}\mathbf{B}(\{\boldsymbol{u},p\},\{\boldsymbol{v},q\}) &= \rho\int_\Omega \frac{\partial \boldsymbol{u}}{\partial t}\cdot\boldsymbol{v}d\Omega + \rho\int_\Omega (\boldsymbol{u}\cdot\nabla)\boldsymbol{u}\cdot\boldsymbol{v}d\Omega - \int_\Omega p(\nabla\cdot\boldsymbol{v})d\Omega \\ &+ 2\mu\int_\Omega \boldsymbol{\varepsilon}(\boldsymbol{u}):\boldsymbol{\varepsilon}(\boldsymbol{v})d\Omega + \int_\Omega (\nabla\cdot\boldsymbol{u})qd\Omega + \int_{\Gamma_O}(\boldsymbol{\sigma}\boldsymbol{u})\cdot\boldsymbol{v}d\Gamma - \rho\int_\Omega \boldsymbol{f}\cdot\boldsymbol{v}d\Omega.\end{aligned} \tag{7}$$

The functional spaces V, V_0 and P are defined in details in Reference 16. Based on the resistance boundary condition $p_i = R_iQ_i$, the stress tensor (2) and $Q_i(\boldsymbol{x},t) = \int_{\Gamma_{O_i}} \boldsymbol{u}\cdot\boldsymbol{n}_i d\Gamma$, we have.[30]

$$\int_{\Gamma_O}(\boldsymbol{\sigma}\boldsymbol{n})\cdot\boldsymbol{v}d\Gamma = \sum_{i=1}^{m}\int_{\Gamma_{O_i}}\left(-R_i\int_{\Gamma_{O_i}}\boldsymbol{u}\cdot\boldsymbol{n}_i d\Gamma\boldsymbol{I} + 2\mu\boldsymbol{\varepsilon}(\boldsymbol{u})\right)\boldsymbol{n}_i\cdot\boldsymbol{v}d\Gamma. \tag{8}$$

The computational domain Ω is covered with a fully unstructured tetrahedral mesh on which we introduce $P_1 - P_1$ finite element spaces V^h, V_0^h and P^h as the counterparts of their infinite dimensional spaces, the semi-discretized system of the Navier–Stokes equations with the stabilization can be described as: Find $\boldsymbol{u}^h \in V^h$ and $p^h \in P^h$ such that $\forall \boldsymbol{v}^h \in V_0^h$ and $\forall q^h \in P^h$,

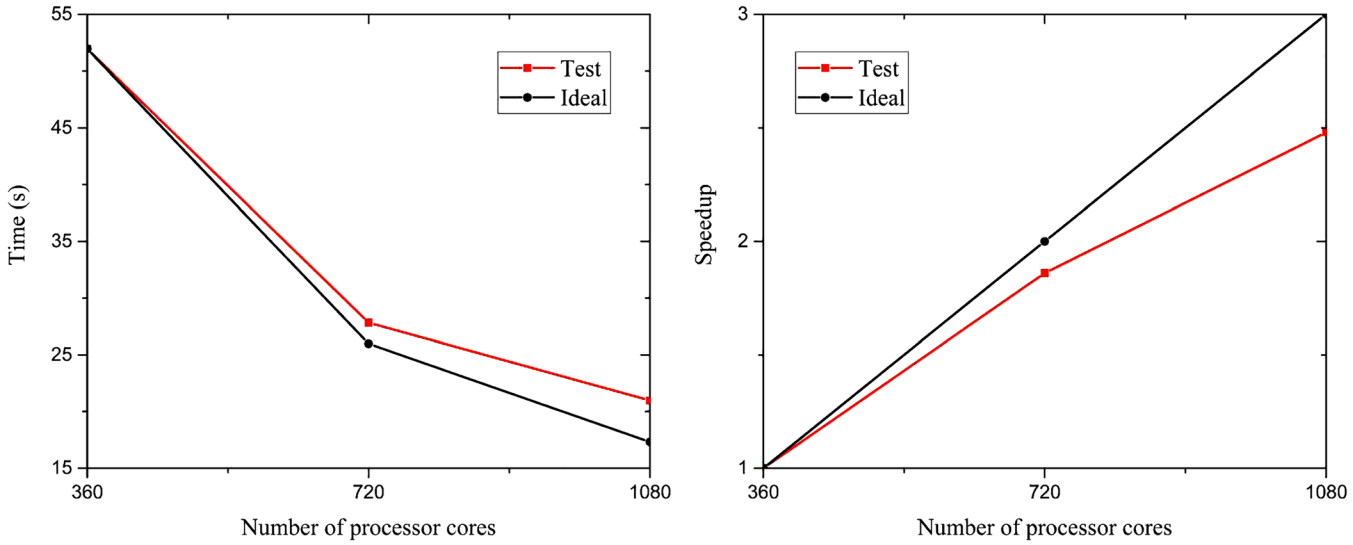

FIGURE 14 The illustrations of compute time versus the number of processor cores (left figure) and speedup versus the number of processor cores (right figure) for the flow in the portal vein. The mesh has 6.99×10^6 elements and the time-step size $\Delta t = 1.00 \times 10^{-3}$ s

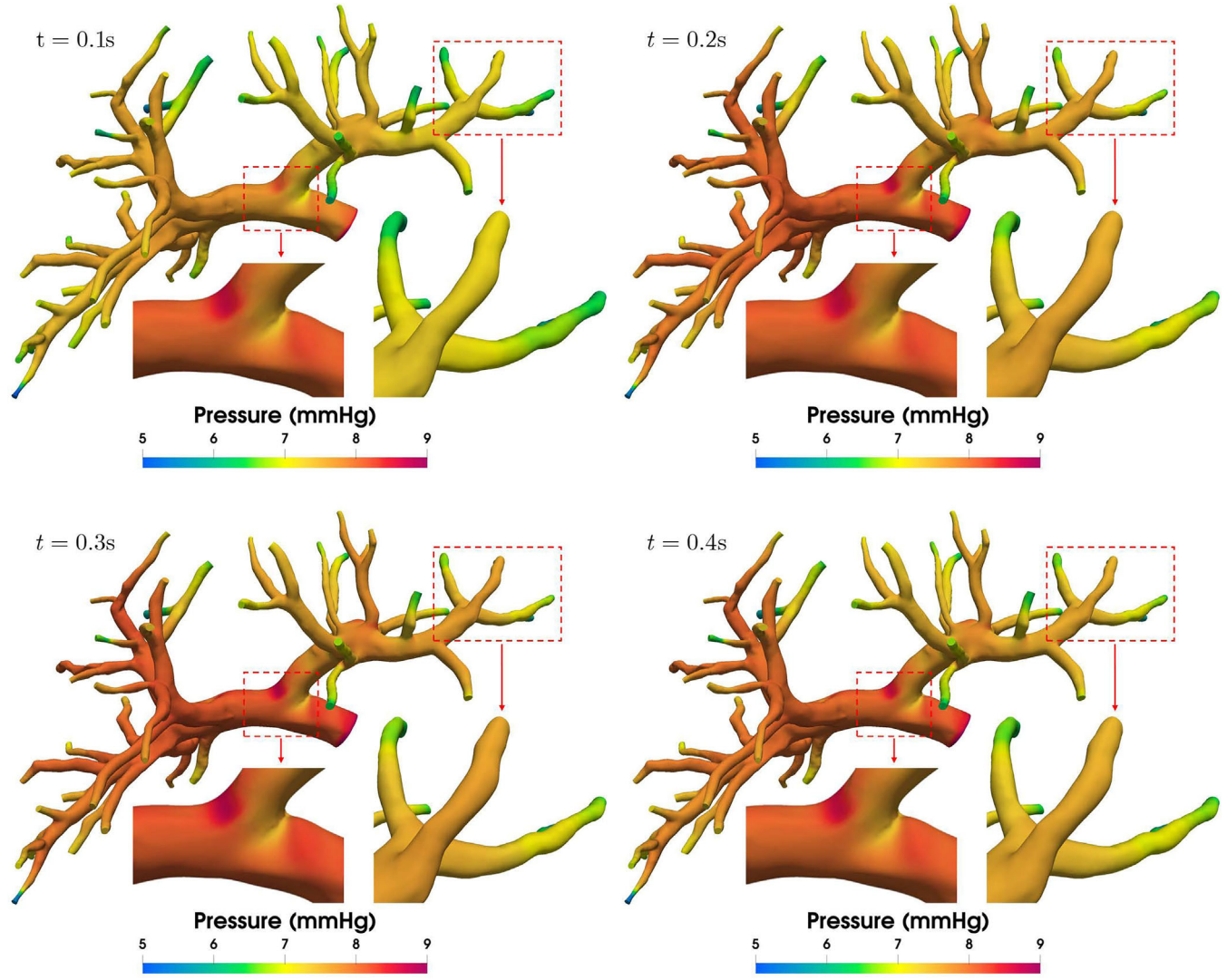

FIGURE 15 The pressure distribution of the computed flow in the hepatic portal vein at various times

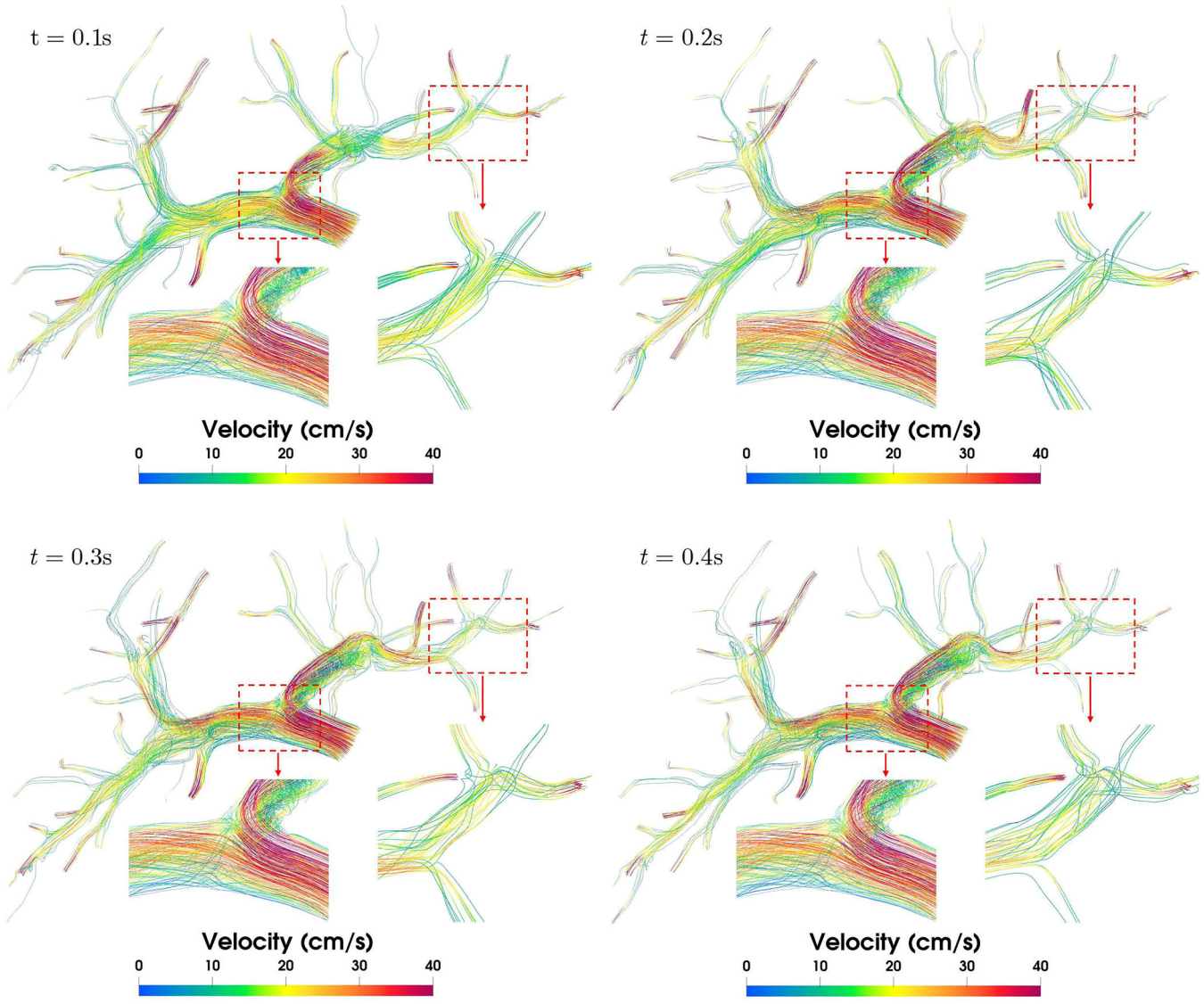

FIGURE 16 The velocity distribution of the computed flow in the hepatic portal vein at various times

$$\mathbf{B}_S\left(\{\boldsymbol{u}^h, p^h\}, \{\boldsymbol{v}^h, q^h\}\right) = 0, \tag{9}$$

with

$$\begin{aligned}\mathbf{B}_S\left(\{\boldsymbol{u}^h, p^h\}, \{\boldsymbol{v}^h, q^h\}\right) &= \mathbf{B}\left(\{\boldsymbol{u}^h, p^h\}, \{\boldsymbol{v}^h, q^h\}\right) \\ &+ \sum_{K\in\ \Omega_h} \left(\rho\frac{\partial \boldsymbol{u}^h}{\partial t} + \rho(\boldsymbol{u}^h\cdot\nabla)\boldsymbol{u}^h + \nabla p^h - \boldsymbol{f}^h, \tau_m\left((\boldsymbol{u}^h\cdot\nabla)\boldsymbol{v}^h + \nabla q^h\right)\right)_K \\ &+ \sum_{K\in\ \Omega_h} \left(\nabla\cdot\boldsymbol{u}^h, \tau_c\nabla\cdot\boldsymbol{v}^h\right)_K,\end{aligned} \tag{10}$$

where the stabilization parameters τ_m and τ_c are defined in Reference 20.

Then Equation (9) can be rewritten as a time-dependent semi-discretized nonlinear system

$$\frac{d\boldsymbol{\mathcal{X}}(t)}{dt} = \mathcal{N}(\boldsymbol{\mathcal{X}}), \tag{11}$$

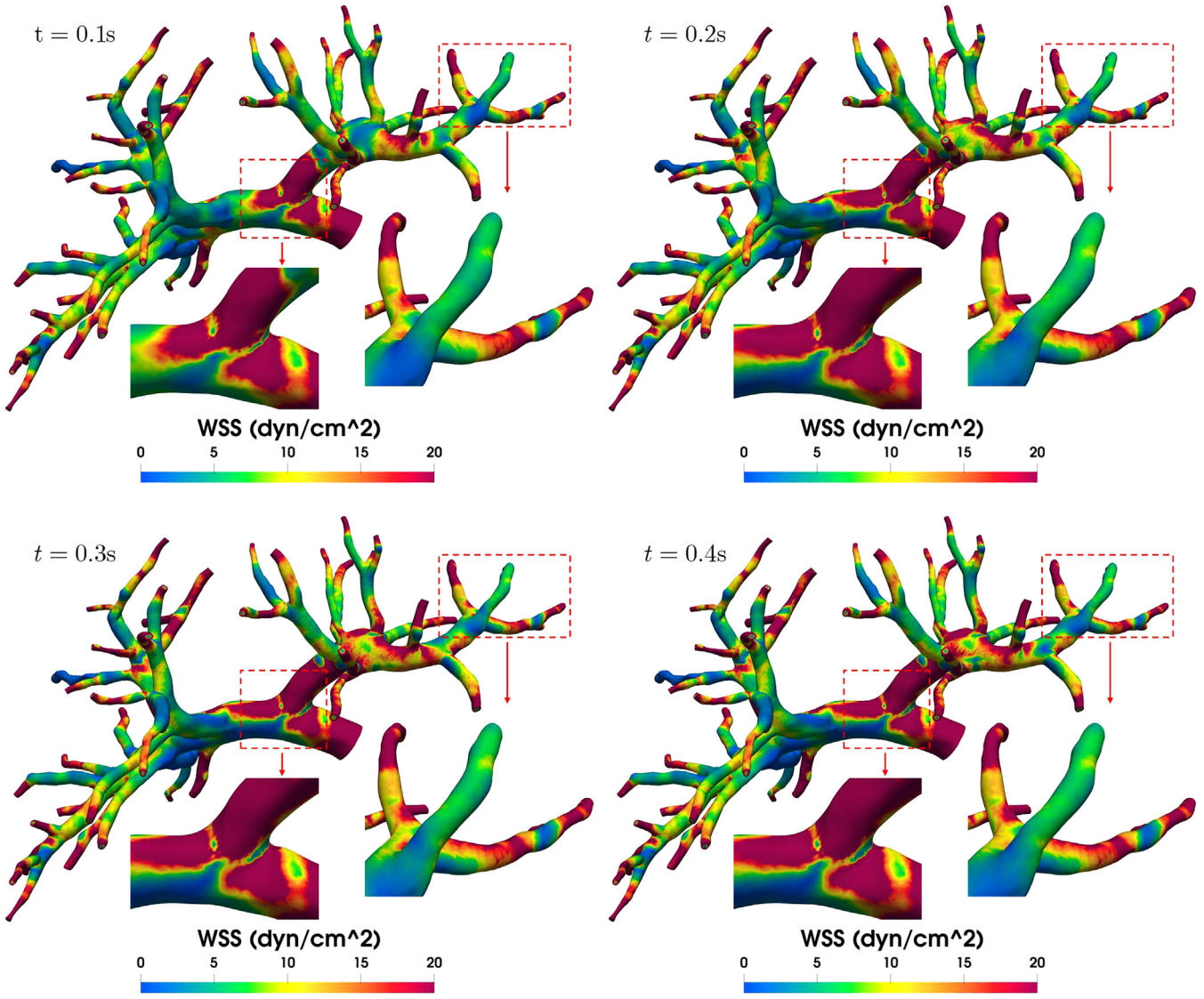

FIGURE 17 The WSS distribution of the computed flow in the hepatic portal vein at various times

where $\boldsymbol{\mathcal{X}}(t)$ is the vector of the nodal values of the velocity $\boldsymbol{u}$ and pressure p, $\mathcal{N}(\cdot)$ is the nonlinear function representing the spatial discretization of Equation (10). Equation (11) can be further discretized by the fully implicit backward Euler method in time

$$\frac{\boldsymbol{\mathcal{X}}^n - \boldsymbol{\mathcal{X}}^{n-1}}{\Delta t} = \mathcal{N}(\boldsymbol{\mathcal{X}}^n), \tag{12}$$

where $\boldsymbol{\mathcal{X}}^n$ is the value of $\boldsymbol{\mathcal{X}}(t)$ at the n-th time step and Δt is the time step size.

For simplicity, Equation (12) can be rearranged to the following nonlinear system

$$\mathcal{F}^n(\boldsymbol{\mathcal{X}}^n) = 0 \tag{13}$$

to be solved at each time step.

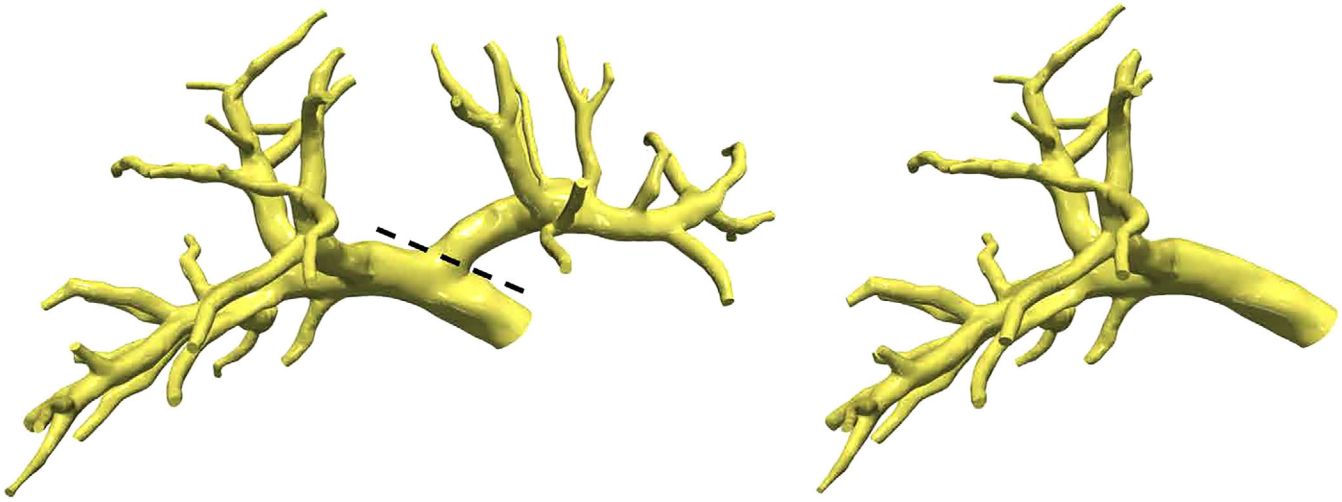

FIGURE 18 Schematic of the preoperative (left figure) and postoperative (right figure) hepatic portal vein

2.3 | Newton-Krylov-Schwarz algorithm

In this section, we briefly describe the Newton-Krylov-Schwarz algorithm[30] for solving the nonlinear system (13). The algorithm includes three components, an inexact Newton[25] as the nonlinear solver, a preconditioned Krylov subspace method (GMRES)[26] as the linear solver at each Newton step, and an overlapping Schwarz method[27] as the preconditioner. The overall algorithm is summarized in Algorithm 1.

Algorithm 1. Newton-Krylov-Schwarz (NKS)

Set the relative tolerances ξ for the linear solver and η for the nonlinear solver;
for *each time step $n = 1, 2, \cdots$,* ***do***
Use the previous time step solution as the initial guess $\boldsymbol{\mathcal{X}}_0^n = \boldsymbol{\mathcal{X}}^{n-1}$
for *each Newton step $k = 0, 1, 2, \cdots$,* ***do***

- *Construct the complete Jacobian matrix $\boldsymbol{J}_k^n$ and setup the restricted additive Schwarz preconditioner $\left(\boldsymbol{M}_k^n\right)^{-1}$*
- *Compute the Newton correction step $\boldsymbol{S}_k^n$ by iteratively solving the preconditioned Jacobian system until it satisfies $||\boldsymbol{J}_k^n\left(\boldsymbol{M}_k^n\right)^{-1}\boldsymbol{M}_k^n\boldsymbol{S}_k^n + \mathcal{F}^n\left(\boldsymbol{\mathcal{X}}_k^n\right)||\leq\xi||\mathcal{F}^n\left(\boldsymbol{\mathcal{X}}_k^n\right)||$*
- *Calculate the step length τ_k^n by a cubic line search*
- *Update the solution with $\boldsymbol{\mathcal{X}}_{k+1}^n = \boldsymbol{\mathcal{X}}_k^n + \tau_k^n\boldsymbol{S}_k^n$ until it satisfies $||\mathcal{F}^n\left(\boldsymbol{\mathcal{X}}_{k+1}^n\right)||\leq\eta||\mathcal{F}^n\left(\boldsymbol{\mathcal{X}}_0^n\right)||$*

end for
Store the converged $\boldsymbol{\mathcal{X}}_{k+1}^n$ as the solution $\boldsymbol{\mathcal{X}}^n$
end for

Here $\boldsymbol{J}_k^n$ is the Jacobian matrix $\nabla\mathcal{F}^n\left(\boldsymbol{\mathcal{X}}_k^n\right)$ which is large, sparse, and highly ill-conditioned. A strong and parallel preconditioner $\left(\boldsymbol{M}_k^n\right)^{-1}$ for the Jacobian matrix is vital because it guarantees the convergence and the robustness of GMRES. The overlapping restricted additive Schwarz (RAS) preconditioner $\left(\boldsymbol{M}_k^n\right)^{-1}$ is constructed as follows. First, we partition the computational domain Ω into n_p non-overlapping subdomains Ω_i ($i = 1, 2, \cdots, n_p$), where n_p equals to the number of processor cores of the parallel machine. Then, each subdomain is extended to Ω_i^δ by including δ layers of mesh elements from its adjacent subdomains. Here, δ is an integer indicating the level of overlap.

On each overlapping subdomain Ω_i^δ, we define the restriction operator $\boldsymbol{R}_i^\delta$ to be the matrix that maps the global vector of unknowns in Ω to those belonging to Ω_i^δ, such that

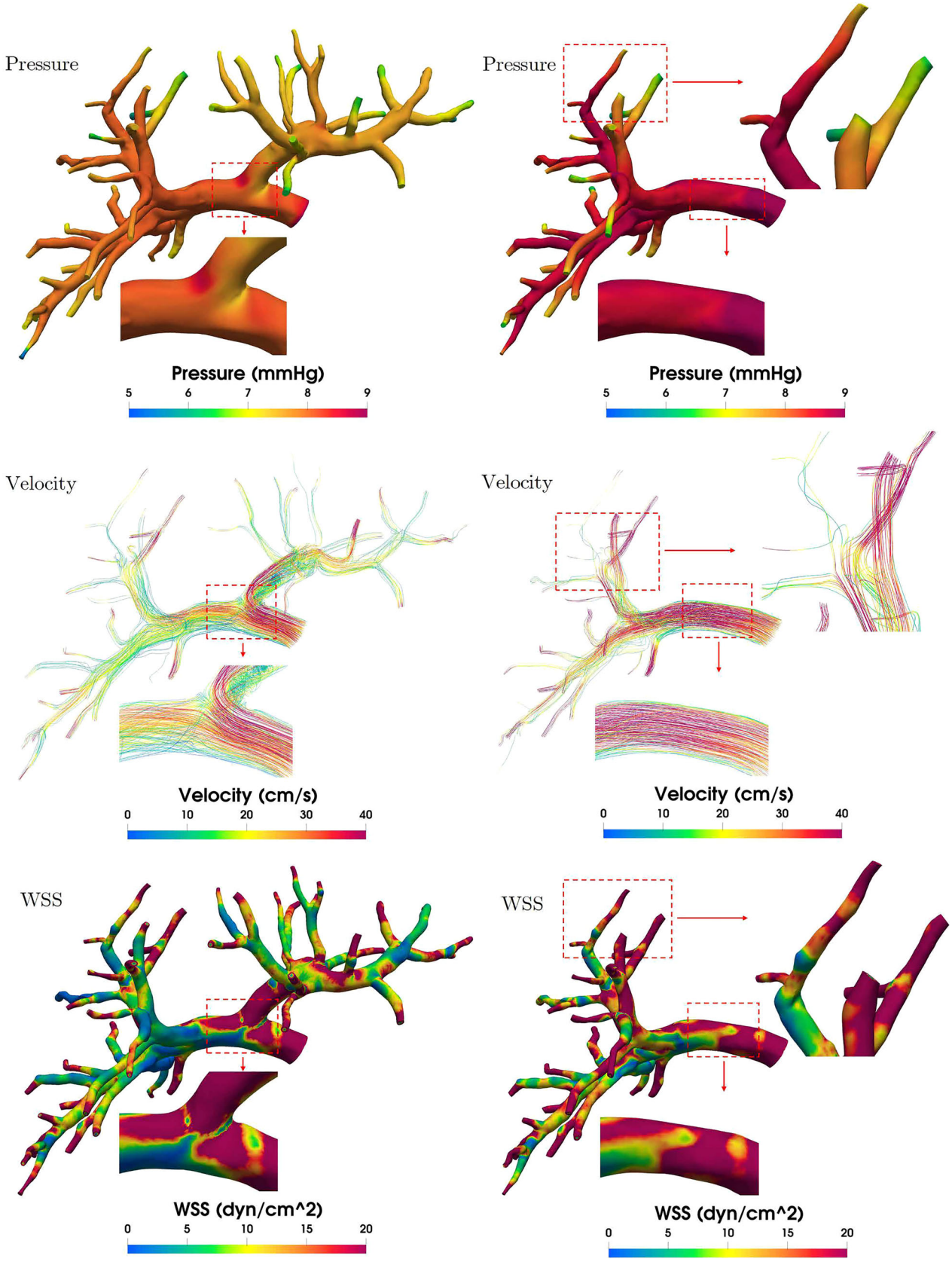

FIGURE 19 The comparisons of the preoperative (left figures) and postoperative (right figures) hepatic portal venous pressure, velocity and WSS distribution at $t = 0.2\ s$

$$\boldsymbol{x}_i^{\delta} = \boldsymbol{R}_i^{\delta}\boldsymbol{x} = (\boldsymbol{I} \;\; \boldsymbol{0}) \begin{pmatrix} \boldsymbol{x}_i^{\delta} \\ \boldsymbol{x} \backslash \boldsymbol{x}_i^{\delta} \end{pmatrix}, \tag{14}$$

here $\boldsymbol{x}\backslash\boldsymbol{x}_i^{\delta}$ means the unknowns outside the subdomains Ω_i^{δ}. We then construct a subdomain Jacobian matrix by

$$\boldsymbol{J}_{k,i}^{n,\delta} = \boldsymbol{R}_i^{\delta}\boldsymbol{J}_k^n\left(\boldsymbol{R}_i^{\delta}\right)^T, i = 1, 2, \cdots, n_p, \tag{15}$$

which is the restriction of the global Jacobian matrix $\boldsymbol{J}_k^n$ to the subdomain Ω_i^{δ}. Here $\left(\boldsymbol{R}_i^{\delta}\right)^T$ is the extension operator, which is defined as the transpose of the restriction operator $\boldsymbol{R}_i^{\delta}$. Using these definitions, the RAS preconditioner is defined as:

$$\left(\boldsymbol{M}_k^n\right)^{-1} = \sum_{i=1}^{n_p} \left(\boldsymbol{R}_i^0\right)^T \left(\boldsymbol{J}_{k,i}^{n,\delta}\right)^{-1} \boldsymbol{R}_i^{\delta}, \tag{16}$$

where $\boldsymbol{R}_i^0$ is the restriction operator to the unknowns in the non-overlapping subdomain Ω_i, defined similarly as $\boldsymbol{R}_i^{\delta}$, and $\left(\boldsymbol{J}_{k,i}^{n,\delta}\right)^{-1}$ is the subspace inverse of the subdomain Jacobian $\boldsymbol{J}_{k,i}^{n,\delta}$. In our application, the linear system corresponding to $\left(\boldsymbol{J}_{k,i}^{n,\delta}\right)^{-1}$ is solved with a point-block incomplete LU (ILU) factorization with some levels of fill-ins.

A sample mesh for the hepatic artery is shown in Figure 3, together with a sample partition by ParMETIS[24] into five overlapping sub-meshes highlighted by different colors. Note that we allocate each sub-mesh to a processor and roughly the same number of elements are included in each sub-mesh to ensure load balance.

3 | NUMERICAL EXPERIMENTS

In this section, we present some numerical experiments for blood flows in the three hepatic vessels, i.e., hepatic artery, portal vein and hepatic vein, and also the parallel performance of the algorithm with respect to the number of processor cores. The main quantities of interests consist of the pressure, the velocity and the wall shear stress (WSS) defined as

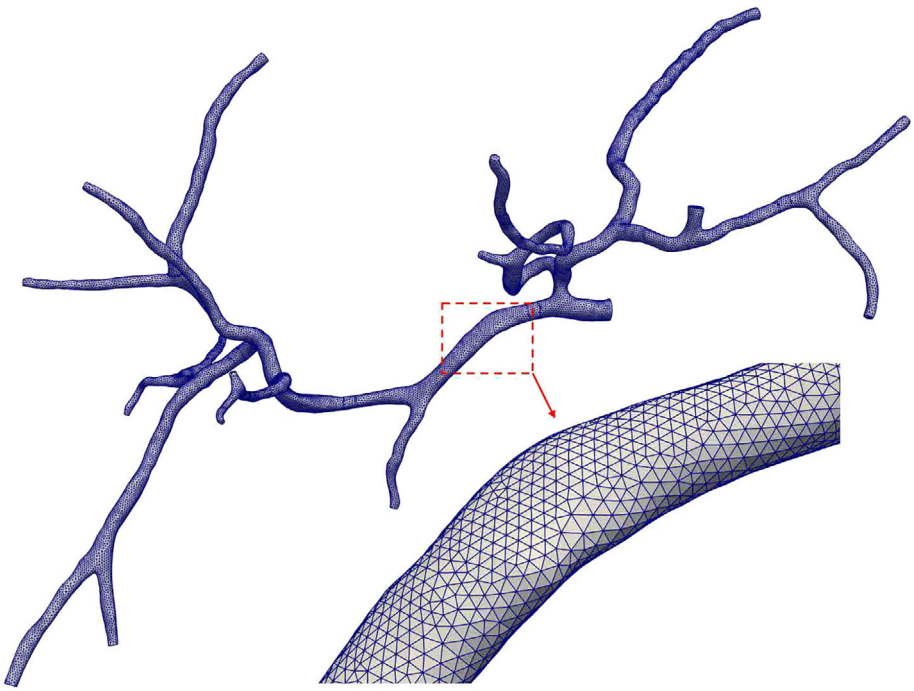

FIGURE 20 A finite element mesh for the hepatic artery

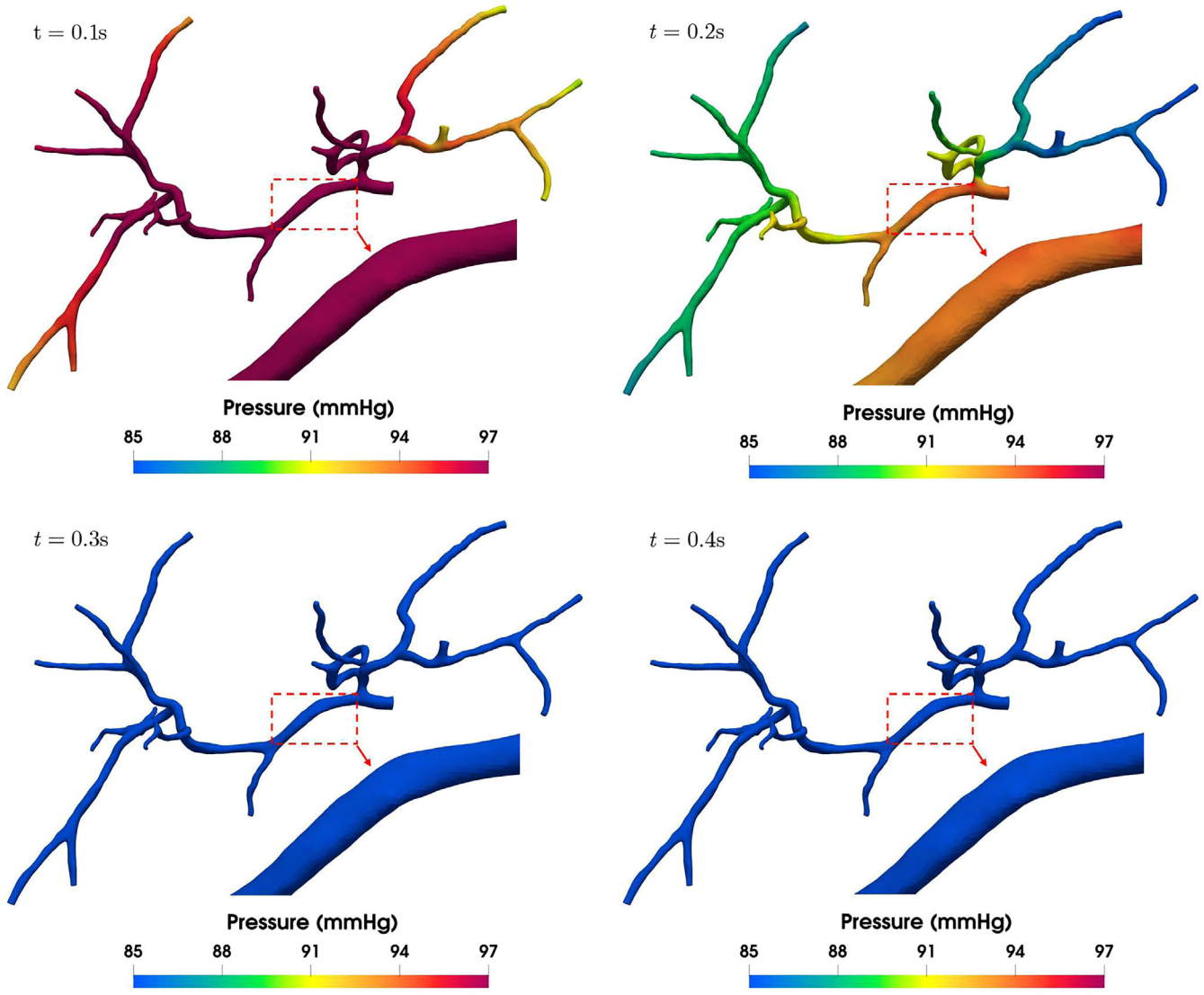

FIGURE 21 The pressure distribution of the computed flow in the hepatic artery at various times

$$\mathrm{WSS} = \boldsymbol{\sigma n} - (\boldsymbol{\sigma n}\cdot\boldsymbol{n})\boldsymbol{n}, \tag{17}$$

where $\boldsymbol{n}$ is the outward normal vector of the wall.

The flow velocities at the inlets of the hepatic artery and the portal vein and the outlet of the hepatic vein are clinically measured by ultrasound[8] as shown in Figure 4, and they are used as the boundary conditions. Note that significant pulsatility of the hepatic arterial blood flow is clearly observed and the velocity curves of the portal vein and the hepatic vein are relatively flat.

In all the numerical experiments, $\rho = 1.05\ g/cm^3$ and $\mu = 0.038\ cm^2/s$[8] are used to characterize the properties of the hepatic blood. In Table 1, we summarize the physiological ranges of hepatic hemodynamics. Note that the values of the hepatic arterial pressure and velocity are larger than the values of portal venous.

The algorithm is implemented using the Portable Extensible Toolkit for Scientific computation (PETSc) library.[36] For this experiment, the relative stopping condition for Newton is 1.0×10^{-6} and the relative stopping condition for GMRES is set to be 1.0×10^{-4}. Incomplete LU (ILU) is used to solve the subdomain problems in the additive Schwarz preconditioner. "ILU(l)" denotes ILU with l level of fill-ins, "np" denotes the number of processor cores, "Newton" denotes the average number of Newton iterations per time step, "GMRES" denotes the average number of GMRES iterations per Newton step, "Time" denotes the average wall clock time in seconds spent per time step, "Memory" stands for the memory consumption in megabyte per processor core per time step, "Speedup" denotes the speedup ratio and "Efficiency" means the parallel efficiency.

3.1 | Comparison with previously published results

To validate the proposed method, we consider an artificial case introduced in Reference 8 as a benchmark problem. Based on the geometric information provided in Appendix A of Reference 8, the tube-shape hepatic artery is reconstructed as shown in Figure 5, and covered by a conformal tetrahedral mesh. The total number of elements is 1.26×10^6, the largest size of the elements is 0.45 *mm*, the smallest is 0.09 *mm* and the average is 0.27 *mm*. The velocity profile in Figure 4A is utilized as the inlet boundary condition. The computed pressure field at $t = 0.16$ *s* is illustrated in Figure 6 (right figure). Comparing with the previously published result shown in Figure 6 (left figure),[8] we see that they are quite similar.

3.2 | The portal vein

In this section we discuss some numerical experiments for the simulation of the blood flow in the portal vein discretized by a finite element mesh as shown in Figure 7. The hepatic portal vein has 1 inlet and 42 outlets. The inflow velocity boundary condition is given in Figure 4B and the total resistance R is chosen such that the computed pressures are within the ranges of typical values in adults.

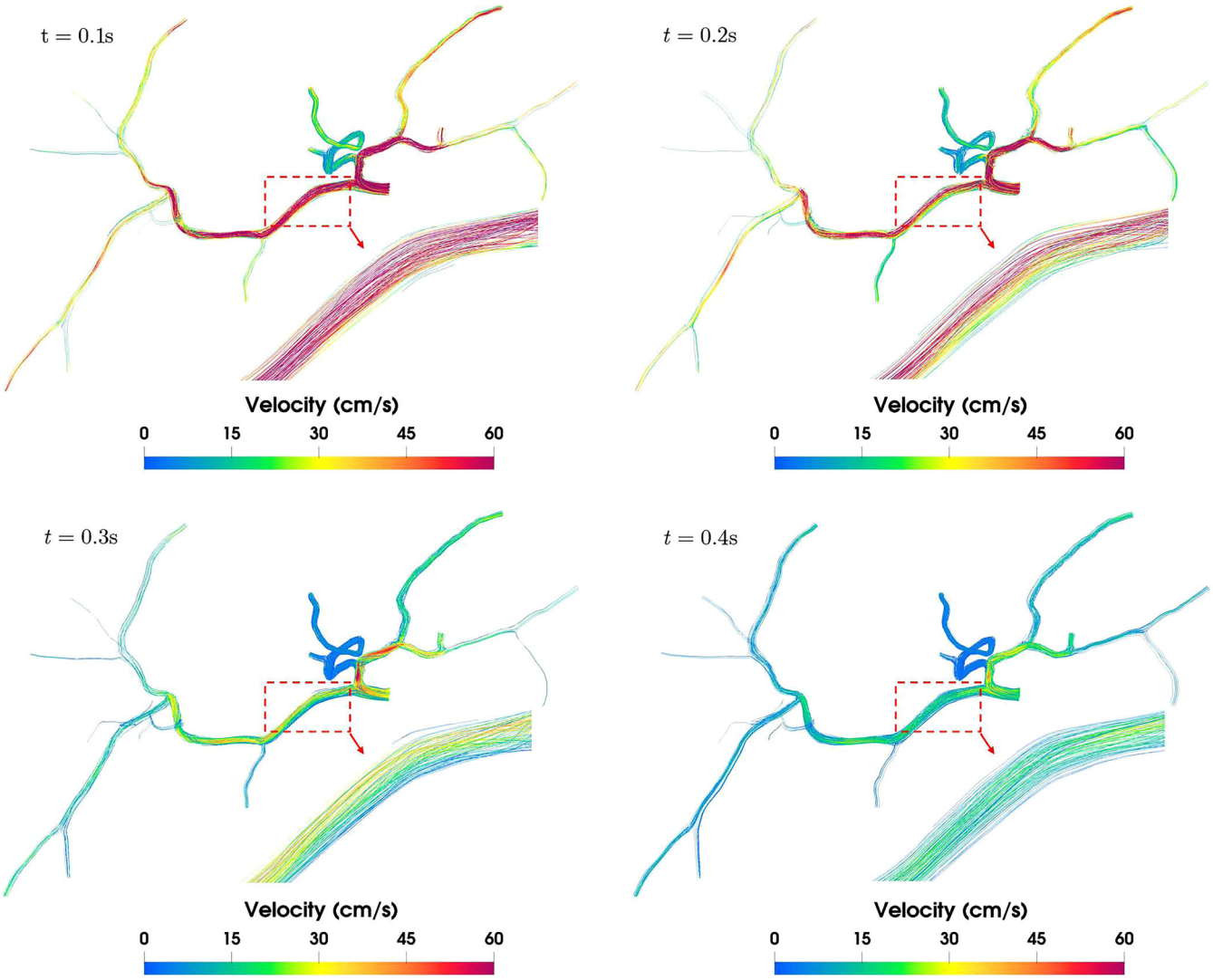

FIGURE 22 The velocity distribution of the computed flow in the hepatic artery at various times

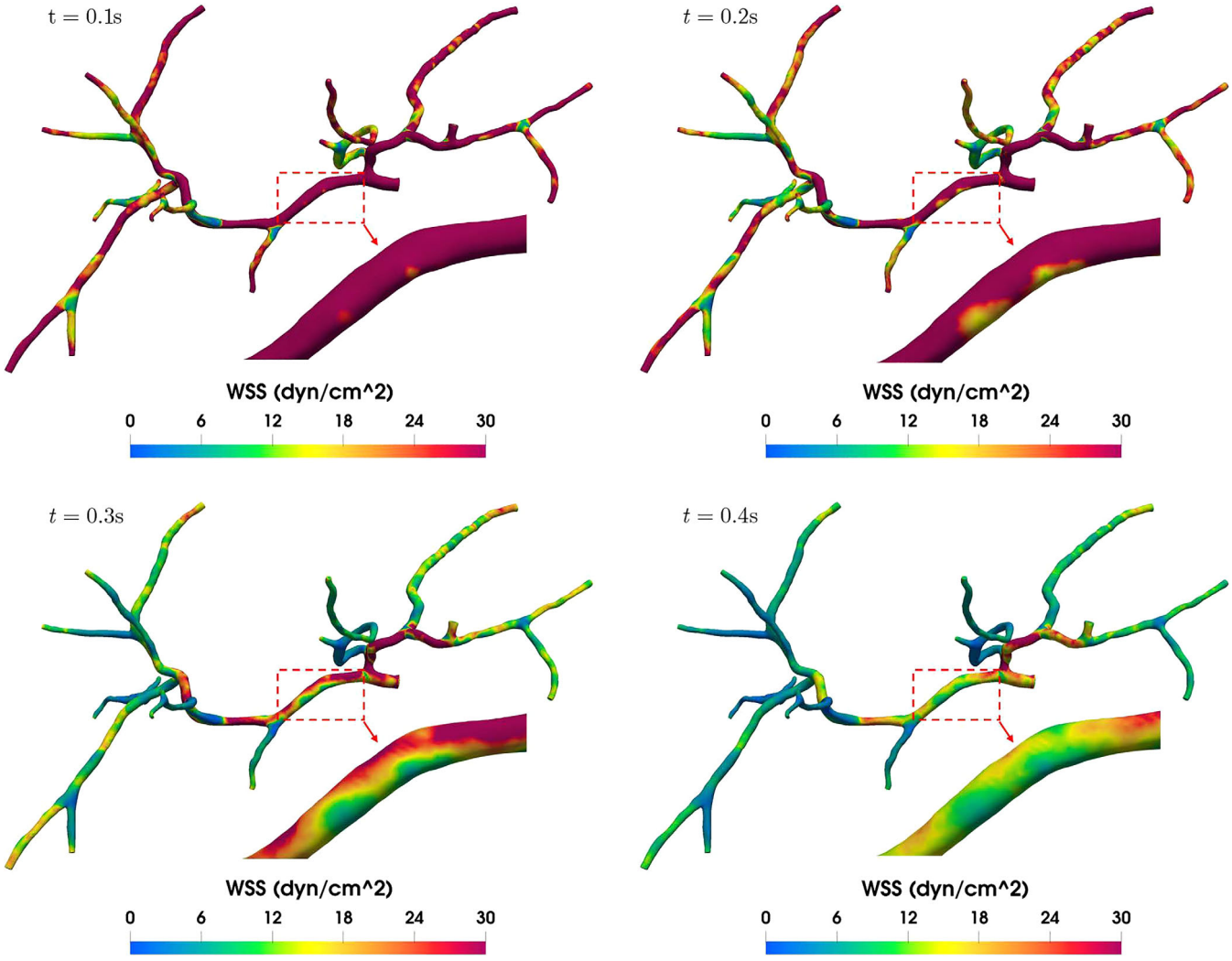

FIGURE 23 The WSS distribution of the computed flow in the hepatic artery at various times

The impact of resistance boundary condition. We study the influence of R to the computed pressure and flow rate. We use a mesh with 2.20×10^6 elements and a time step size $\Delta t = 1.0 \times 10^{-3}$. In Figure 8, the computed flow rate and pressure at three different points, located at near the inlet (P1), near an outlet to the right of the figure (P2) and in the middle of a branch to the left of the figure (P3), are plotted to show for four different $R = 200\ dyn/(s \cdot cm^5)$, $300\ dyn/(s \cdot cm^5)$, $400\ dyn/(s \cdot cm^5)$ and $500\ dyn/(s \cdot cm^5)$. From Figure 8, we see that the resistance has slight influence to the flow rate, but significant influence to the pressure. When R equals to $300\ dyn/(s \cdot cm^5)$, the computed flow rate and pressure are both within the normal ranges shown in Table 1. Thus, $R = 300\ dyn/(s \cdot cm^5)$ will be used in the subsequent portal venous experiments. Moreover, the results for three cardiac cycles are plotted in Figure 8 to illustrate the influence of the initial value to the computed results. From Figure 8, we see that the influence is not significant beyond the first time step because we use a fully implicit and coupled algorithm.

For the simulation, it is important to determine the right mesh size and the right time step size so that the desired features of the solution are captured and the overall compute time is minimized. For this purpose, we test several different meshes and several time step sizes below.

Mesh convergence study. In Figure 9, the computed flow rate and pressure at three different points are plotted to understand the convergent properties with respect to the four progressively refined meshes with 3.40×10^5, 6.90×10^5, 1.35×10^6 and 2.20×10^6 elements. The time step size is $\Delta t = 1.0 \times 10^{-3}$. We can observe that the gap between the red line (2.20×10^6 elements) and the dotted blue line (1.35×10^6 elements) is quite small. This means either of the meshes is acceptable for this problem, but the other two meshes are too coarse to produce an accurate solution. In Figures 10-12, , we present the other computed fields including the pressure, the velocity and the wall shear stress at one particular

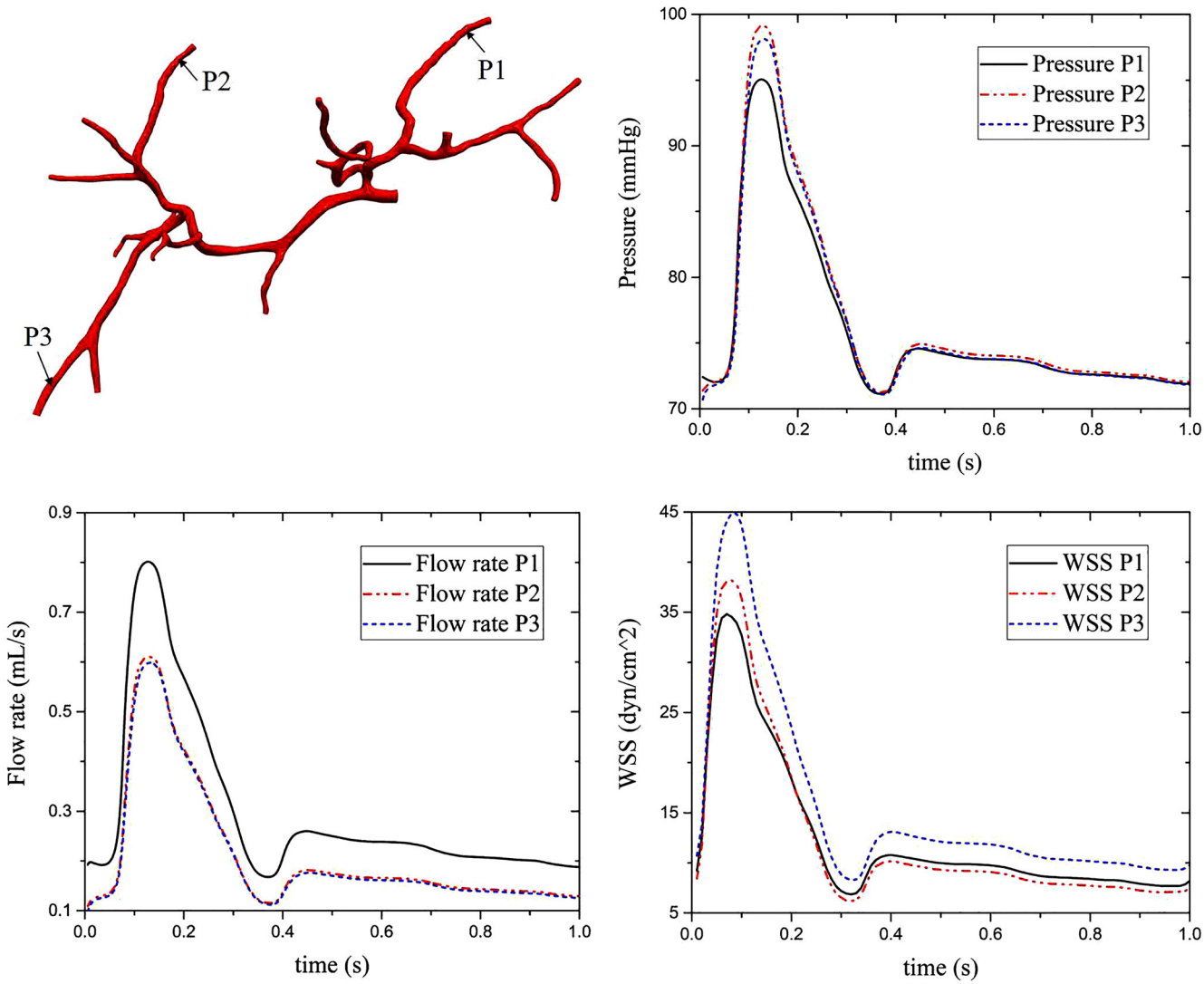

FIGURE 24 A comparison of computed pressure, flowrate and WSS values for three selected points in hepatic artery

time step using these meshes. We can see that the numerical solution converges when the number of elements of the mesh increases.

The impact of time step sizes. To understand the time accuracy and the performance of the proposed method with respect to the time step size, we fix the mesh to be the one with 2.20×10^6 elements and consider four time step sizes $\Delta t = 5.00 \times 10^{-2}$, 1.00×10^{-2}, 5.00×10^{-3} and 1.00×10^{-3}. From Table 2, we see clearly that smaller time step size results in fewer iterations of GMRES, smaller total compute time per time step and less memory. In Figure 13, the flow rate and pressure at three different points are plotted to show the convergence properties with different time step sizes. The error for $\Delta t = 5.00 \times 10^{-2}$ is large but the gaps between the other three lines are quite small. This means that any time step sizes smaller than or equal to $\Delta t = 1.00 \times 10^{-2}$ is acceptable.

The impact of overlapping sizes and subdomain solvers. The level of fill-in in the ILU factorization of the subdomain matrices and the overlapping size of the subdomains of the Schwarz preconditioner make significant influences on the parallel performance of the algorithm. Table 3 shows the results of various fill-in levels and overlapping sizes. From Table 3 we observe that the increase of overlapping size from 0 to 2 reduces the computing time and a further increase from 2 to 4 increases the computing time. Therefore 2 is the optimal value of the overlap for this numerical experiment. Furthermore, when we fix the overlapping size to 2, we note that the increase of the fill-in level from 1 to 4 increases the computing time. Following the observations, ILU(1) and overlapping size 2 will be used in all the subsequent experiments.

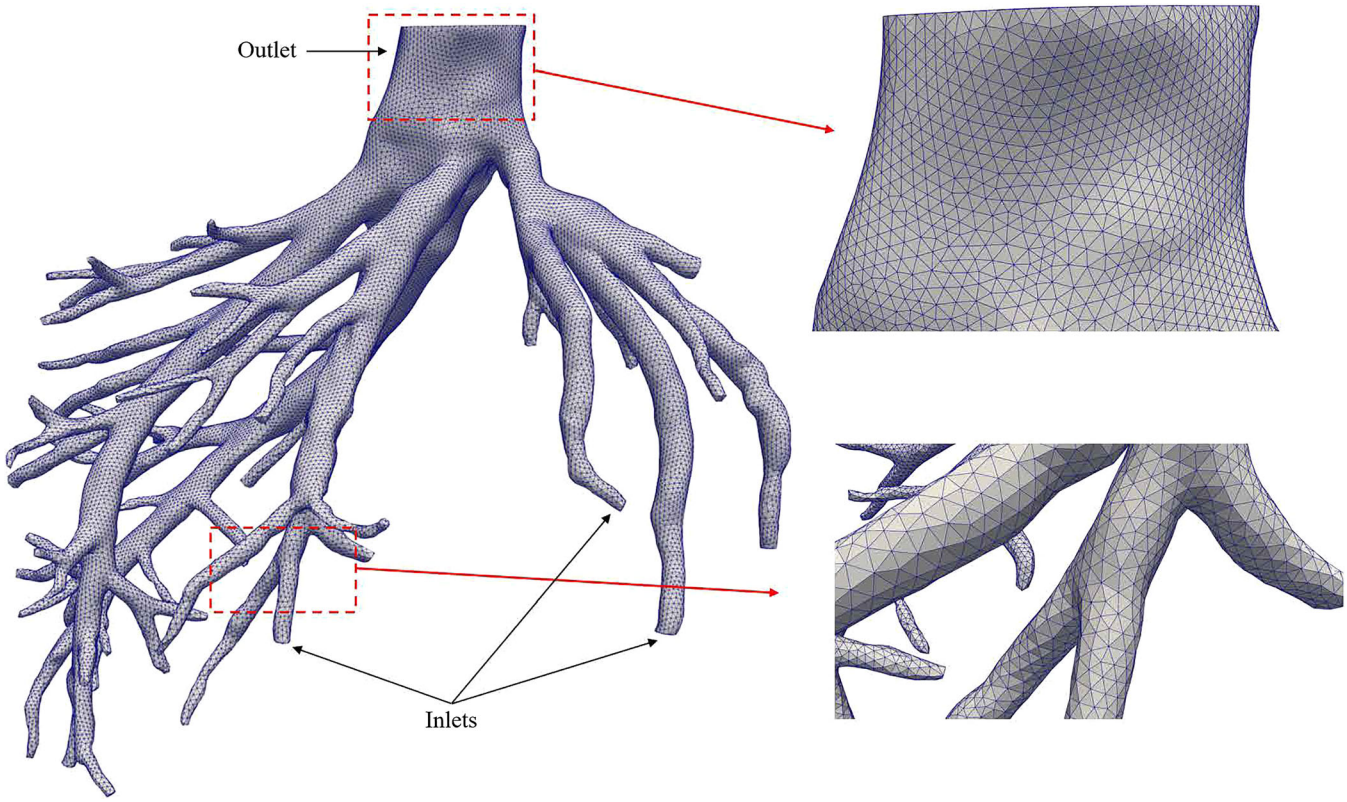

FIGURE 25 A sample mesh for the hepatic vein

A parallel scalability study. The experiments are carried out on a supercomputer, and each compute node of the computer has two Intel Xeon E5-2692v2 12-core 2.2GHz processors and 64GB of shared memory. Table 4 and Figure 14 present the performance of the algorithm in terms of the number of Newton iterations per time step, the number of GMRES iterations per Newton step, the total compute time per time step, the total memory per processor core per time step, the speedup ratio and the parallel efficiency. The calculations are done using a mesh with 6.99×10^6 elements, where the largest size of the elements is 1.25 *mm*, the smallest is 0.13 *mm* and the average is 0.34 *mm*. The time step size $\Delta t = 1.00 \times 10^{-3}$ *s*, the subdomain solver is ILU(1) and the overlapping size is 2. We see clearly that the linear and nonlinear algebraic solvers are both scalable in the sense that the number of Newton iterations and GMRES iterations change very little as the number of processor cores increase. It can be seen that when the number of processor cores increases from 360 to 1080, the compute time reduces to 20.98 *s* and the parallel efficiency reduces to 83%, which is quite good considering the fact that the geometry of the problem is rather complicated.

The numerical results at various time. The pressure, velocity and WSS distributions of the blood flow in the hepatic portal vein at various times ($t = 0.1$ *s*, 0.2 *s*, 0.3 *s* and 0.4 *s*) are illustrated in Figures 15–17. We can see that the amplitudes of the pressure, velocity and WSS change very little due to the fact that the input pulsatile velocity shown in Figure 4B is flat.

3.3 | The portal vein after a left hepatectomy

Hepatic resection is one of the most efficient and frequently-used surgery to treat advanced liver diseases such as hepatic tumors and intrahepatic gall stones. The preoperative and postoperative schematics of the left hepatectomy are shown in Figure 18. The corresponding veins are used as the computational domain in the next set of numerical experiments. Hepatectomy often causes several syndromes, for example, the overall resistance of the resected liver to blood flow is greater than that of a full liver, and this may result in high blood pressure in the sinusoids, leading to damage of the liver.[37]

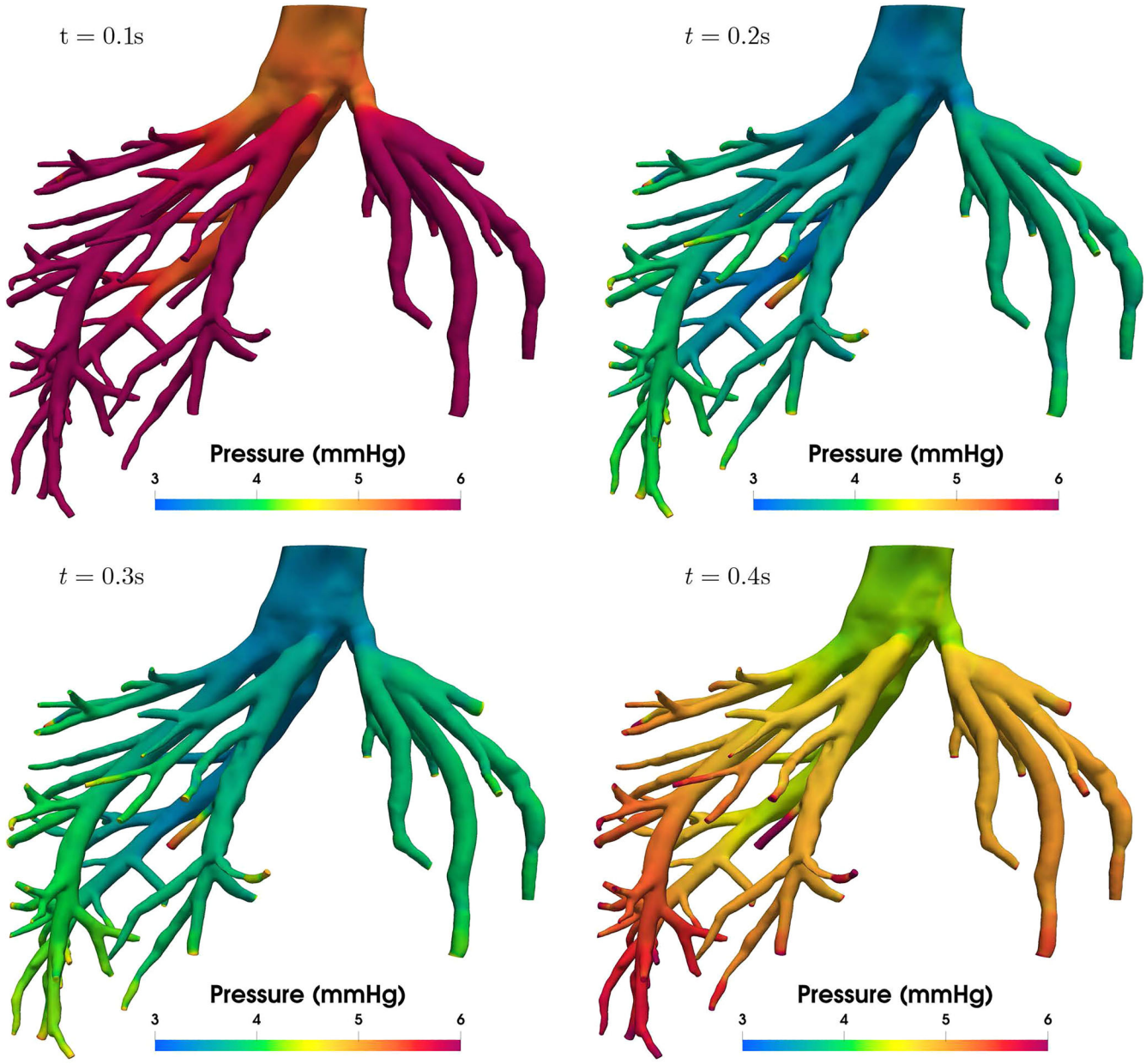

FIGURE 26 The pressure distribution of the computed flow in the hepatic vein at various times

In this experiment, we present the change of the hepatic hemodynamics after the left hepatectomy, in particular, we compute the pressure, the velocity and the WSS of the flows before and after the left hepatectomy. From Figure 19 we see that the values of the pressure, velocity and WSS are all within the normal ranges before the hepatectomy, when compared with the normal values in Table 1. However, they are beyond the normal range after the hepatectomy, suggesting certain medical intervention is necessary after the surgery.

3.4 | The hepatic artery

In this section we focus on the blood flow in the hepatic artery, which includes 1 inlet and 16 outlets. The inlet velocity is prescribed in Figure 4A and a total resistance $R = 8000\ dyn/(s \cdot cm^5)$ is assumed for this test. We use a mesh with 4.0×10^5 elements (see Figure 20), the largest size of the elements is 0.66 mm, the smallest is 0.12 mm and the average

is 0.37 *mm*. The time step size $\Delta t = 1.0 \times 10^{-3}$, all other settings are the same as in the experiments in the previous section.

In Figure 21, we show the pressure distribution of the hepatic artery at four selected times including early ($t = 0.1\ s$), mid ($t = 0.2\ s$), late ($t = 0.3\ s$) systole and diastole ($t = 0.4\ s$) respectively. Additionally, the velocity and WSS distributions at the corresponding times are also presented in Figures 22 and 23. From Figures 21–23, we observe that the values of pressure, velocity and WSS are significantly different at the crest ($t = 0.2\ s$) and the trough ($t = 0.4\ s$). To better understand the change of the pressure, the flow rate and WSS in time we plot the solution at three different points as marked in Figure 24. It is clearly shown that the waveforms match the input pulsatile velocity profile in Figure 4A.

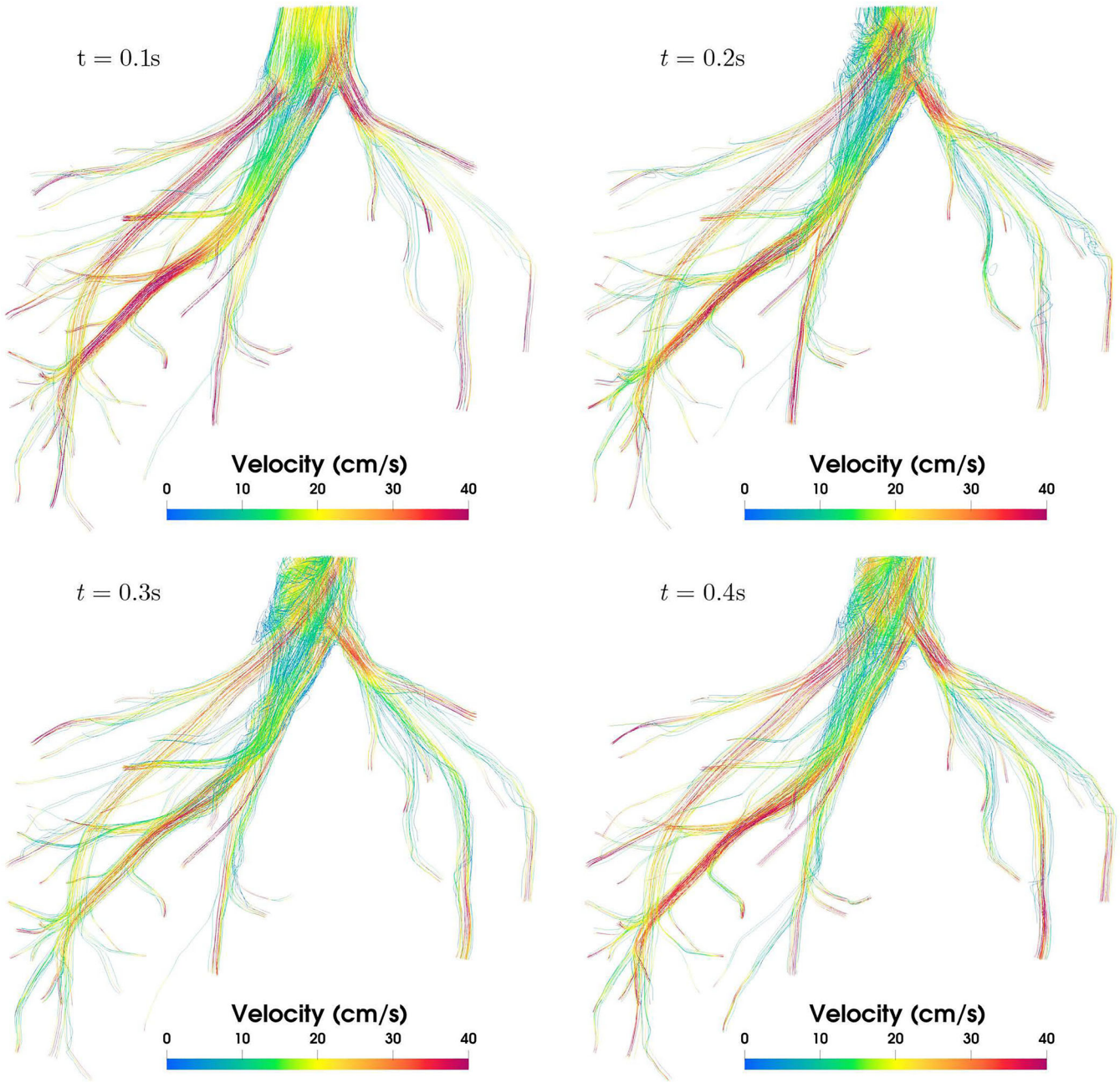

FIGURE 27 The velocity distribution of the computed flow in the hepatic vein at various times

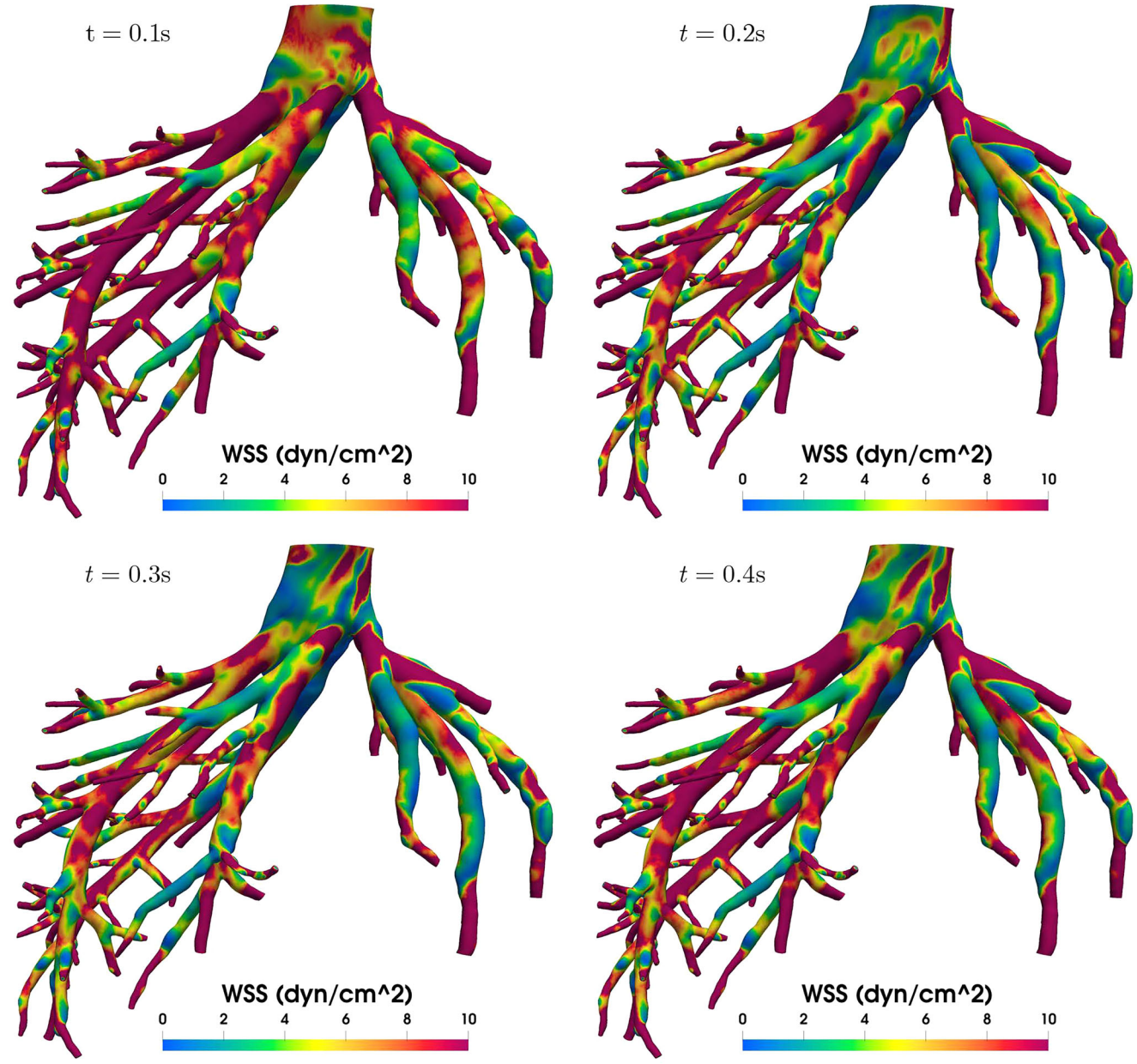

FIGURE 28 The WSS distribution of the computed flow in the hepatic vein at various times

3.5 | The hepatic vein

In this section we study the hepatic vein using a mesh with 3.9×10^5 elements as shown in Figure 25. Comparing with the hepatic artery and the hepatic portal vein that have one inlet and multi-outlets, the hepatic vein has multiple inlets and only one outlet, whose corresponding boundary conditions are given in Equation (5). The computed pressure, velocity and WSS distribution at various time are presented in Figures 26–28. Comparing with the hepatic vein plotted in Figures 26–28 with the portal vein plotted in Figures 15–17 and the hepatic artery plotted in 21, 22, 23, we can see the values of the pressure, velocity and WSS in the small vessels are larger than the values at the large vessels, this distribution is opposite with the portal vein and hepatic artery. The reason is that the hepatic vein transports blood from the small vessels to the large vessels. Since the hepatic venous pulsatile velocity shown in Figure 4C is relative flat in a cardiac cycle, the changes of the pressure, velocity and WSS at various time are not obvious.

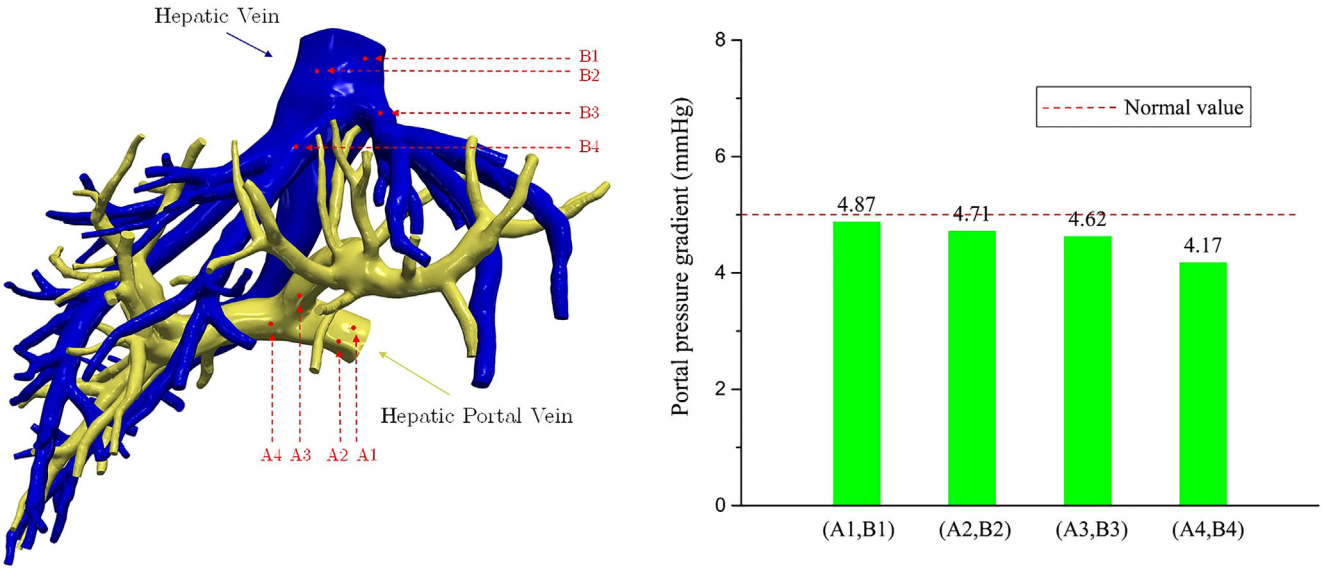

FIGURE 29 The left figure shows the sample pairs of points for calculating the PPG at the portal vein and the hepatic vein. The right figure shows the computed time-averaged PPG values for these pairs of points

3.6 | The portal pressure gradient

As mentioned in the introduction, PPG measures the degree of portal hypertension and is a prognostic indicator in liver disease.[38] In clinical practice, PPG is obtained by interventional radiology which is a rather complicated procedure. In this section we provide a pilot study about obtaining a numerical approximation of PPG based on the calculations presented in earlier sections of the paper. We pick several pairs of points (A1,B1), (A2,B2), (A3,B3) and (A4,B4) as marked in Figure 29 to compute the difference in the pressure between the portal vein and the hepatic vein, i.e., the PPG, for a cardiac cycle. Their time-averaged values are presented in the right figure of Figure 29. It is clear that all four approximations are within the normal ranges as indicated in Table 1. Note that the study is to show the capability of the proposed algorithm, and the comparison with clinical measurements is beyond the scope of the present work.

4 | CONCLUSIONS

Blood flows in the full hepatic vessels including the hepatic artery, the hepatic portal vein and the hepatic vein are simulated in this work based on the patient-specific geometry segmented from the CT images of an adult liver. To compute the blood flows, a scalable parallel method is used to implicitly solve the unsteady incompressible Navier–Stokes equations discretized with a stabilized finite element method on fully unstructured meshes. The parallel algebraic solver includes an Newton method, a Krylov subspace method (GMRES) and an overlapping Schwarz preconditioner. The pressure, velocity and WSS of the blood flows in the hepatic artery, hepatic portal vein and hepatic vein are computed, and their values are all within the ranges of healthy patients. Such a flow analysis for a full cardiac cycle takes about 5 h of time on a parallel computer with about 1000 processor cores without counting the time spent on the image segmentation and the mesh generation. Furthermore, the robustness of the algorithm with respect to the mesh sizes and the time step sizes are investigated. Moreover, the parallel scalability is also studied with up to 1080 processor cores and 83% parallel efficiency is archived. As applications of the proposed method, we computed the blood flows in the portal vein before and after a left hepatectomy and calculated the PPG values at some selected pairs of points. As expected from previous clinical studies, the pressure after the surgery is much higher than the preoperative pressure. The algorithm/software developed in the paper is a valuable non-invasive tool for the planning of liver surgery if more case studies confirm the results of the present work.

Although blood flows in the three-dimensional patient-specific hepatic artery, portal vein and hepatic vein are all simulated in this work, but they are calculated separately. A full hepatic blood flow modeling including the hepatic

artery, portal vein, hepatic vein and hepatic tissue would be more interesting. Under this circumstance, the outlets of the hepatic artery and portal vein and the inlets of the hepatic vein are connected to the hepatic tissue by virtue of the interface condition instead of the artificial outlet boundary conditions.

ACKNOWLEDGMENTS

This research was supported in part by the National Key R&D Program of China under 2018YFE0198400, China Postdoctoral Science Foundation under 2020M682960, SIAT Innovation Program for Excellent Young Researchers, NSFC under 81871447 and 11801543 and Shenzhen grant under ZDSYS201703031711426.

CONFLICT OF INTEREST

The authors declare no conflict of interest.

ORCID

Xiao-Chuan Cai https://orcid.org/0000-0003-0296-8640

REFERENCES

1. Lautt WW. Hepatic circulation: physiology and pathophysiology. Morgan & Claypool Publishers 2009;1(1):1-174.
2. Amsel S. *Liver Structures and Functions - A Closer Look (Advanced)*. Exploring Nature Educational Resource; 2020. http://www.exploringnature.org/db/view/Liver-Structures-and-Functions-A-Closer-Look-Advanced.
3. Wang FS, Fan JG, Zhang Z, Gao B, Wang HY. The global burden of liver disease: the major impact of China. *Hepatology*. 2014;60(6):2099-2108.
4. Berzigotti A, Seijo S, Reverter E, Bosch J. Assessing portal hypertension in liver diseases. *Expert Rev Gastroenterol Hepatol*. 2013;7(2):141-155.
5. Kong FD, Kheyfets V, Finol E, Cai XC. Simulation of unsteady blood flows in a patient-specific compliant pulmonary artery with a highly parallel monolithically coupled fluid-structure interaction algorithm. *Int J Numer Method Biomed Eng*. 2019;35(7):e3208.
6. Umbarkar TS, Kleinstreuer C. Computationally efficient fluid-particle dynamics simulations of arterial systems. *Commun Comput Phys*. 2015;17(2):401-423.
7. Ho H, Sorrell K, Peng LQ, Yang Z, Holden A, Hunter P. Hemodynamic analysis for transjugular intrahepatic portosystemic shunt (TIPS) in the liver based on a CT-image. *IEEE Trans Med Imaging*. 2012;32(1):92-98.
8. Ma RF, Hunter P, Cousins W, Ho H, Bartlett A, Safaei S. Anatomically based simulation of hepatic perfusion in the human liver. *Int J Numer Method Biomed Eng*. 2019;35(9):e3229.
9. Ma RF, Hunter P, Cousins W, Ho H, Bartlett A, Safaei S. Modeling the hepatic arterial flow in living liver donor after left hepatectomy and postoperative boundary condition exploration. *Int J Numer Method Biomed Eng*. 2020;36(3):e3268.
10. Basciano CA, Kleinstreuer C, Kennedy AS, Dezarn WA, Childress E. Computer modeling of controlled microsphere release and targeting in a representative hepatic artery system. *Ann Biomed Eng*. 2010;38(5):1862-1879.
11. Aramburu J, Anton R, Rivas A, Ramos JC, Sangro B, Bilbao JI. Computational particle-haemodynamics analysis of liver radioembolization pretreatment as an actual treatment surrogate. *Int J Numer Method Biomed Eng*. 2017;33(2):e02791.
12. Aramburu J, Anton R, Rivas A, Ramos JC, Sangro B, Bilbao JI. The role of angled-tip microcatheter and microsphere injection velocity in liver radioembolization: a computational particle-hemodynamics study. *Int J Numer Method Biomed Eng*. 2017;33(12):e2895.
13. Yin XP, Huang X, Li Q, et al. Hepatic hemangiomas alter morphometry and impair hemodynamics of the abdominal aorta and primary branches from computer simulations. *Front Physiol*. 2018;9:334.
14. Sheu TWH, Chou CW, Tsai SF, Liang PC. Three-dimensional analysis for radio-frequency ablation of liver tumor with blood perfusion effect. *Comput Methods Biomech Biomed Engin*. 2005;8(4):229-240.
15. Stoter SKF, Muller P, Cicalese L, Tuveri M, Schillinger D, Hughes TJR. A diffuse interface method for the Navier-Stokes/Darcy equations: perfusion profile for a patient-specific human liver based on MRI scans. *Comput Methods Appl Mech Eng*. 2017;321:70-102.
16. Kong FD, Kheyfets V, Finol E, Cai XC. An efficient parallel simulation of unsteady blood flows in patient-specific pulmonary artery. *Int J Numer Meth Biomed Eng*. 2018;34(4):e2952.
17. Xiao N, Humphrey JD, Figueroa CA. Multi-scale computational model of three-dimensional hemodynamics within a deformable full-body arterial network. *J Comput Phys*. 2013;244:22-40.
18. Forti D, Quarteroni A, Deparis S. A parallel algorithm for the solution of large-scale nonconforming fluid-structure interaction problems in hemodynamics. *J Comput Math*. 2017;35(3):363-380.
19. Luo L, Shiu WS, Chen RL, Cai XC. A nonlinear elimination preconditioned inexact Newton method for blood flow problems in human artery with stenosis. *J Comput Phys*. 2019;399:108926.
20. Chen RL, Wu YQ, Yan ZZ, Zhao Y, Cai XC. A parallel domain decomposition method for 3D unsteady incompressible flows at high Reynolds number. *J Sci Comput*. 2014;58(2):275-289.
21. Liao ZJ, Chen RL, Yan ZZ, Cai XC. A parallel implicit domain decomposition algorithm for the large eddy simulation of incompressible turbulent flows on 3D unstructured meshes. *Int J Numer Meth Fluids*. 2019;89(9):343-361.

22. Smith B, Bjorstad P, Gropp W. *Domain Decomposition: Parallel Multilevel Methods for Elliptic Partial Differential Equations*. New York: Cambridge University Press; 2004.
23. Toselli A, Widlund O. *Domain Decomposition Methods: Algorithms and Theory*. Vol 34. Dordrecht, the Netherlands: Springer Science & Business Media; 2006.
24. Karypis G, Kumar V. Multilevelk-way partitioning scheme for irregular graphs. *J Parallel Distrib Comput*. 1998;48(1):96-129.
25. Eisenstat SC, Walker HF. Choosing the forcing terms in an inexact Newton method. *SIAM J Sci Comput*. 1996;17(1):16-32.
26. Saad Y, Schultz MH. GMRES: a generalized minimal residual algorithm for solving nonsymmetric linear systems. *SIAM J Sci Stat Comput*. 1986;7(3):856-869.
27. Cai XC, Sarkis M. A restricted additive Schwarz preconditioner for general sparse linear systems. *SIAM J Sci Comput*. 1999;21(2):792-797.
28. Vignon-Clementel IE, Figueroa CA, Jansen KE, et al. Outflow boundary conditions for three-dimensional finite element modeling of blood flow and pressure in arteries. *Comput Methods Appl Mech Eng*. 2006;195(29-32):3776-3796.
29. Taylor CA, Fonte TA, Min JK. Computational fluid dynamics applied to cardiac computed tomography for noninvasive quantification of fractional flow reserve: scientific basis. *J Am Coll Cardiol*. 2013;61(22):2233-2241.
30. Wu YQ, Cai XC. A parallel two-level method for simulating blood flows in branching arteries with the resistive boundary condition. *Comput. Fluids*. 2011;45(1):92-102.
31. Yu HB, Bartlett A, Hunter P, Ho H. Computational simulations for the hepatic arterial buffer response after liver graft transplantation from an adult to a child. *Med Eng Phys*. 2020;75:49-52.
32. Tanaka MDK, Mitsui K, Morimoto M, et al. Increased hepatic arterial blood flow in acute viral hepatitis: assessment by color doppler sonography. *Hepatology*. 1993;18(1):21-27.
33. Eipel C, Abshagen K, Vollmar B. Regulation of hepatic blood flow: the hepatic arterial buffer response revisited. *World J Gastroenterol*. 2010;16(48):6046-6057.
34. Iranpour P, Lall C, Houshyar R, et al. Altered Doppler flow patterns in cirrhosis patients: an overview. *Ultrasonography*. 2016;35(1):3-12.
35. Kumar A, Sharma P, Sarin SK. Hepatic venous pressure gradient measurement: time to learn. *Indian J Gastroenterol*. 2008;27(2):74-80.
36. Balay S, Abhyankar S, Adams MF, et al. PETSc Users Manual. Technical Report, Argonne National Laboratory; 2020.
37. Dahmen U, Hall CA, Madrahimov N, Milekhin V, Dirsch O. Regulation of hepatic microcirculation in stepwise liver resection. *Acta Gastroenterol Belg*. 2007;70(4):345-351.
38. Huang JY, Samarasena JB, Tsujino T, et al. EUS-guided portal pressure gradient measurement with a simple novel device: a human pilot study. *Gastrointest Endosc*. 2017;85(5):996-1001.

How to cite this article: Lin Z, Chen R, Gao B, et al. A highly parallel simulation of patient-specific hepatic flows. *Int J Numer Meth Biomed Engng*. 2021;37:e3451. https://doi.org/10.1002/cnm.3451